Relaxation of Energy Constraints for Positrons Generating the Galactic Annihilation Signal

Souradeep Das [1,2,*] Mark R. Krumholz [1,†]
Roland M. Crocker [1,‡] Thomas Siegert [3,§] and Laura Eisenberger [3,¶]
[1] Research School of Astronomy and Astrophysics, Australian National University, 233 Mt Stromlo Road, Stromlo ACT 2611, Australia
[2] Center for High Energy Physics, Indian Institute of Science, C. V. Raman Avenue, Bengaluru 560012, India
[3] Julius-Maximilians-Universität Würzburg, Institut für Theoretische Physik und Astrophysik, Lehrstuhl für Astronomie, Emil-Fischer-Str. 31, D-97074 Würzburg, Germany
(Dated: June 3, 2025)

Even 50 years after the discovery of a positron annihilation line from the inner Galaxy, no class of astrophysical sources has emerged as a definitive explanation for both the emission morphology and flux. Positrons produced by dark matter annihilation or decay have been proposed, but the mass of any such candidate is constrained by continuum γ-ray emission at energies > 511 keV. Earlier analyses have claimed that this emission requires that the positrons have kinetic energies less than a few MeV at injection, disfavoring both much of the dark matter parameter space and many potential compact astrophysical source classes such as pulsars. However, these constraints were not based on a full forward model of the γ-ray line and continuum data, and did not marginalize over uncertainties about the relative angular distributions of the line and continuum. Here we describe an improved analysis that overcomes these limitations, and show that constraints on the injection energy are much weaker than previously claimed; even under conservative assumptions the data are consistent with initial energies up to ~ 50 MeV.

INTRODUCTION

The 511 keV γ-ray line observed in the inner Galaxy remains a compelling mystery more than 50 years after its discovery [1–8]. Its luminosity implies the existence of a mechanism that produces positrons at a rate $\gtrsim 10^{43}$ s^{-1} [8–10]. While radionuclides produced in supernovae can plausibly supply this [9, 11], such a scenario is difficult to reconcile with the observation that a significant fraction of the emission, perhaps as much as half, occurs in the Galactic bulge [10, 12–16] rather than in the disk where most of the young stars and supernovae occur.

These challenges have motivated a variety of alternative scenarios, including positron sources tied to the old stellar populations that dominate the bulge [13, 14, 17, 18], transport of positrons into the bulge [15, 19–24], pair production in jets of compact objects such as millisecond pulsars [25] and microquasars [26–28], and emission from compact binaries [14, 29–32], as well as more exotic scenarios such as decaying or annihilating dark matter [33–40], metastable/excited dark matter [41–47], evaporating primordial black holes [48–52], or a combination of these (e.g., [52–54]). Solutions involving a dark matter or old stellar origin are particularly attractive because they explain the bulge-dominated morphology of the signal [38].

Measurements of continuum radiation around the line constrain these scenarios because positrons injected at relativistic energies interact with the interstellar medium (ISM) through bremsstrahlung, inverse Compton radiation, and "in-flight" annihilation to produce γ-ray continuum emission [9, 55–57]. Higher initial energy-positrons yield stronger continuum radiation, so measurements of the continuum translate directly to upper limits on the initial positron energy. Previous analyses based on this idea have claimed upper bounds of ~ 3 - 7 MeV on the positron initial energy [55, 56], a limit that would exclude both many prospective astrophysical sources (e.g., highly relativistic jets) and much of the parameter space for models in which the positrons are produced by thermal relic dark matter such as Weakly Interacting Massive Particles (WIMPs) [58, 59].

However, the purported limits are sensitive both to the exact values of the γ-ray line and continuum flux – which suffer from large systematic uncertainties due to the complex analysis required to estimate non-point source fluxes – and to estimates of the non-radiative losses (e.g., Coulomb and ionization) that positrons undergo during deceleration from relativistic speeds. These uncertainties motivate us to revisit constraints on the maximum energy of injected positrons, combining an updated treatment of positron energy loss and radiation [60], more recent data from the INTEGRAL satellite processed using significantly improved techniques [10, 61, 62], and full forward-modeling that properly marginalizes over uncertainties in both the data analysis and the astrophysical background. Our analysis shows that upper bounds on the injection energy are significantly weaker than previously claimed, making positrons with injection energies up to $\sim$50 MeV fully consistent with the data.

γ-RAY DATA

The majority of our data come from the SPI instrument aboard the INTEGRAL satellite, which offers 22 broad bins from 30 keV to 8 MeV and two narrow bins centered at 511 keV and 1809 keV to measure the line fluxes due to thermalized positron annihilation and ^{26}Al decay, respectively [62]. Because higher-energy γ-rays help constrain higher injection energies [63], we supplement these data with measurements from COMPTEL and EGRET aboard the CGRO satellite, which provide 3 broad bands from 10 MeV to 300 MeV [56, 64]. A central challenge when combining these data sets is that uncertainties in SPI's background level and photon arrival direction, and to a lesser extent COMPTEL's and EGRET's, make it impossible to extract the total diffuse flux within some specified angular region of the sky in a fully model-independent way. This in turn means that we cannot be sure of the relative normalization of the SPI and CGRO data, a complication that was ignored in earlier analyses. This relative normalization is critical because, as noted above, constraints on the maximum energy of injected positrons come primarily from the relative strengths of the line and continuum.

To handle this uncertainty we use SPI fluxes measured over four regions of interest (ROIs); three circular regions centered on the Galactic center with radii of 5°, 9°, and 18°, and a square region defined by the Galactic coordinates $|l| < 47.5°$ and $|b| < 47.5°$. The fluxes for circular regions are obtained by fitting spatial models to the square region, which we obtain from ref. [62]. These regions cover a range of contributions from the bulge-like and disk-like components of the 511 keV signal, and thus yield a range of line-to-continuum ratios for the SPI data. For the COMPTEL and EGRET data, we use the solid angle-integrated fluxes obtained by ref. [56] for a square region defined by $|l| < 10°$, $|b| < 10°$. Since CGRO/COMPTEL and CGRO/EGRET data do not cover an area that precisely matches any of the ROIs covered by the SPI analyses, we consider three possible strategies to assign these higher-energy fluxes to each ROI: `flat`, whereby we assume that the CGRO fluxes scale linearly with the solid angle of the ROI (corresponding to the fluxes being uniform on the sky), `ptsrc`, whereby we assume that the CGRO fluxes are independent of the solid angle (corresponding to the case where the fluxes arise from a point source at the Galactic center), and `like511`, whereby we assume that the ratio of the CGRO fluxes for different ROIs are identical to the ratios of the 511 keV line fluxes (corresponding to what we would expect if the high-energy fluxes were produced by exactly the same population as produces the 511 keV line). Below we fit our model for each possible combination of ROI and scaling strategy.

FORWARD MODEL FOR THE SPECTRUM

Lepton injection model. Our model includes two sources of leptons: mildly-relativistic positrons injected by β^+ decay of radioactive nuclei, and relativistic e^+/e^- pairs from some other mechanism whose energies at injection $E_{\rm inj}$ we seek to fit. We neglect the fraction α of cases where internal bremsstrahlung (IB) yields injection energies $< E_{\rm inj}$, but we do include the IB emission – see below. We divide β^+ decay into positrons produced by ^{26}Al and by all other candidate astrophysical nuclides (e.g., ^{44}Ti, ^{56}Ni), since ^{26}Al is accompanied by production of 1809 keV photons detectable by SPI. We parameterize the total positron injection rate from all sources as $\dot{n}^{\rm inj}_{e^+}$, the fraction injected by the relativistic source as $f_{\rm rel}$, and the fractions injected by ^{26}Al and all other β^+ sources as $f_{^{26}\rm Al}$ and f_β, respectively. Thus, the differential rate of positron injection at energy E_i is

$$\frac{{\rm d}\dot{n}^{\rm inj}_{\rm e^+}}{{\rm d}E_i} = \dot{n}^{\rm inj}_{\rm e^+}\left[f_{\rm rel}\delta(E_i - E_{\rm inj}) + f_\beta\chi^\beta(E_i) + f_{^{26}\rm Al}\chi^{\rm Al}(E_i)\right] \tag{1}$$

where χ^β and $\chi^{\rm Al}$ are the positron energy distributions produced by ^{44}Ti (or ^{56}Ni) and ^{26}Al decay, respectively, which we take from refs. [6, 11]. The corresponding expression for electron injection is identical, but with $f_\beta = f_{^{26}\rm Al} = 0$.

Leptonic emission. γ-ray emission from injected leptons occurs via four channels. First, IB during pair creation produces a γ-ray spectrum [65, 66]

$$\frac{{\rm d}\dot{n}^{\rm IB}_\gamma}{{\rm d}E_\gamma} = \dot{n}^{\rm inj}_{e^+} f_{\rm rel}\frac{\alpha}{\pi}\frac{1}{E_\gamma}\left[\left[1+\left(\frac{s'}{s}\right)^2\right]\ln\left(\frac{s'}{m_e^2}\right) - 2\frac{s'}{s}\right] \tag{2}$$

where $s = 4E^2_{\rm inj}$ and $s' = 4E_{\rm inj}(E_{\rm inj} - E_\gamma)$. Second, β^+-decay of ^{26}Al produces excited ^{26}Mg nuclei that deexcite via emission of an 1809 keV photon, yielding a spectrum $d\dot{n}^{1809}_\gamma/dE_\gamma = (f_{^{26}\rm Al}\dot{n}^{\rm inj}_{e^+}/0.82)\delta(E_\gamma - 1809\,{\rm keV})$ (corresponding to a 0.82 branching ratio for β^+-decay [6]), where we have approximated the line profile by a δ-function since our bins do not resolve the line shape. Third, leptons traversing the ISM emit cooling radiation via bremsstrahlung, inverse Compton, and, for positrons, in-flight annihilation. Since our ROIs are large and leptonic cooling times are short, all leptons injected in a given ROI likely cool completely within it [67]. Thus the steady-state γ-ray production rate via ISM cooling is

$$\frac{{\rm d}\dot{n}^{{\rm cool},e^\pm}_\gamma}{{\rm d}E_\gamma} = \int {\rm d}E_i\ \frac{{\rm d}\dot{n}^{\rm inj}_{\rm e^\pm}}{{\rm d}E_i}\frac{{\rm d}n^{{\rm cool},e^\pm}_\gamma}{{\rm d}E_\gamma}(E_\gamma;E_i) \tag{3}$$

where ${\rm d}n^{{\rm cool},e^\pm}_\gamma/{\rm d}E_\gamma$ is the number of photons per unit energy E_γ we would expect to be produced by a single positron/electron injected with an initial energy E_i as it cools to non-relativistic energies. We compute this quantity numerically using the CRIPTIC cosmic ray propagation code [60] (see End Matter and Figure S1 of Supplemental Material); this calculation also provides $f_{\rm IFA}(E_i)$, the fraction of positrons of initial energy E_i that suffer in-flight annihilation before thermalizing, which we will require below.

Finally, positrons that cool to thermalize with the ISM annihilate to photons. A fraction $1-f_{\rm Ps} \ll 1$ of these annihilate directly, yielding two 511 keV photons, while the remainder first form *positronium* (Ps) [8, 68], which can be para-Ps (with probability $f_{\rm p} = 25\%$; [69]) or ortho-Ps (probability $f_{\rm o} = 75\%$). The former also decays to two 511 keV photons, while the latter undergoes three-photon decay to form a continuum below 511 keV. The resulting total γ-ray spectrum is

$$\frac{{\rm d}\dot{n}_\gamma^{\rm th}}{{\rm d}E_\gamma} = \dot{n}_{e^+}^{\rm inj}(1-\overline{f}_{\rm IFA}) \times \left[2\left(1-f_{\rm Ps}+f_{\rm p}f_{\rm Ps}\right)\phi(E_\gamma - m_e) + 3 f_{\rm o} f_{\rm Ps}\frac{{\rm d}P^{\rm oPs}}{{\rm d}E_\gamma}\right], \tag{4}$$

where we approximate the line as a Gaussian of width 2 keV (using the line profile ϕ), ${\rm d}P^{\rm oPs}/{\rm d}E_\gamma$ is the oPs continuum profile (which we take from ref. [69]), and $\overline{f}_{\rm IFA}$ is the injection-weighted mean fraction of positrons that undergo in-flight annihilation before thermalizing.

Backgrounds. In addition to emission from injected leptons, our model includes two background contributions: a population of unresolved point sources (UPS) that drive the sharp rise in the spectrum below ≈ 100 keV [70–73], and inverse Compton (IC) emission by higher-energy ($\gtrsim$ GeV) cosmic ray electrons. We describe the background model in the End Matter.

Fitting method. We transform our model for the true spectrum to observed photon fluxes F_E by dividing by $4\pi D^2$, where D is the effective distance to the emission, and then applying the instrument response function of ref. [74] to convert the model fluxes to the corresponding data space bins selected for our SPI analysis. No energy response function is available for COMPTEL or EGRET, so we apply no instrumental correction for them. Our final model has a total of 11 free parameters (see Table A1 of the End Matter) which we constrain using a Markov Chain Monte Carlo fit to the data for each combination of ROI and strategy for relative scaling of CGRO and INTEGRAL fluxes; we take our final result for each ROI from whichever scaling gives the highest Bayes factor (see End Matter). Because our model omits some emission sources that might be non-negligible in the higher-energy CGRO bands (e.g., the low-energy tail of π^0 decay from cosmic ray protons), we treat the CGRO measurements only as upper limits in the fit.

RESULTS

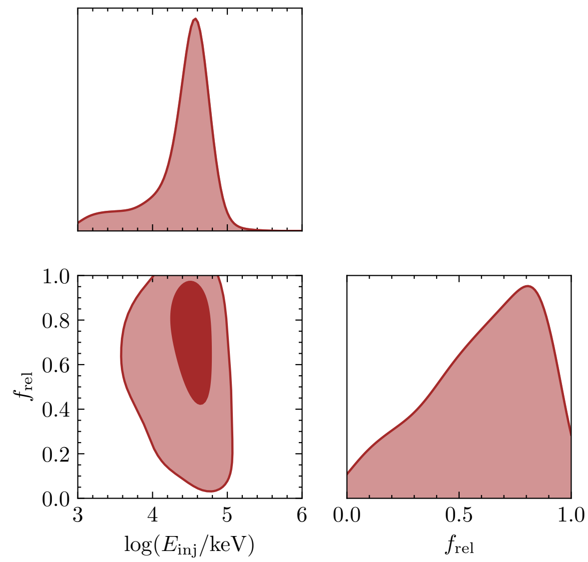

FIG. 1: Posterior distribution for the pair injection energy $E_{\rm inj}$ (in keV) and the fraction of positrons injected relativistically ($f_{\rm rel}$) for the 9° ROI. The shaded region in the off-diagonal subplot shows the 1σ and 2σ bounds on the joint parameter space, while the two diagonal panels show the marginal PDF for each quantity.

We show a corner plot of posteriors derived from our MCMC analysis for the 9° ROI in Figure 1; these fits are for the `ptsrc` scaling, which has marginally the highest Bayes factor, though for this ROI the results are similar regardless of the scaling. We provide a table of Bayes factors for all ROIs, scalings, and full corner plots for the highest Bayes factor models for each ROI in the Supplemental Material. We show a comparison between the observed and MCMC-predicted spectra for this case in Figure 2, demonstrating that our model does a good job of reproducing the observations.

For the model shown in Figure 1, we obtain a 95% confidence upper bound $E_{\rm inj} < 62$ MeV, with the relativistic source providing $f_{\rm rel} \approx 65\%$ of the positrons. In principle the model also requires $E_{\rm inj} > 2$ MeV and $f_{\rm rel} > 14\%$ at 95% confidence, but these lower limits are driven by the need for a relativistic source to contribute to the continuum above the 511 keV line, which Figure 2 shows could come equally well from electrons or positrons. Thus we cannot exclude a model with no relativistic positrons at all (i.e., the 511 keV line is entirely from β^+-decay) but with an additional source of ~ 50 MeV electrons.

Our results presented in the Supplemental Material show that, for other ROIs and varying approaches to computing ISM cooling radiation, we obtain comparable upper bounds on $E_{\rm inj}$ and lower bounds on $f_{\rm rel}$. The case

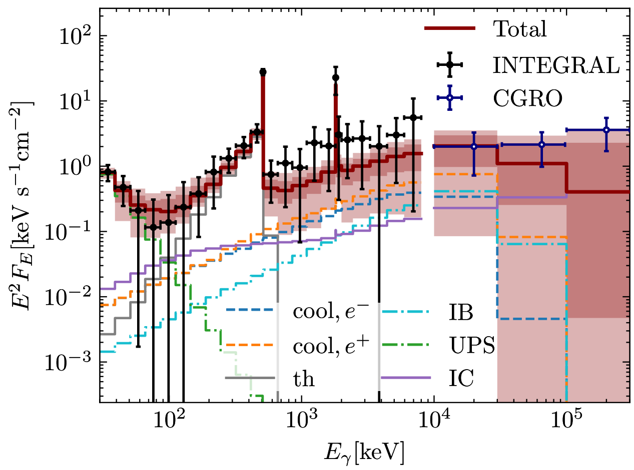

FIG. 2: Fit results for our 9° ROI. Points with error bars show observations, and the solid brown lines and shaded regions show the median and 1σ and 2σ bands of total emission produced by our MCMC fits. Other lines show median contributions from individual emission mechanisms as indicated in the legend.

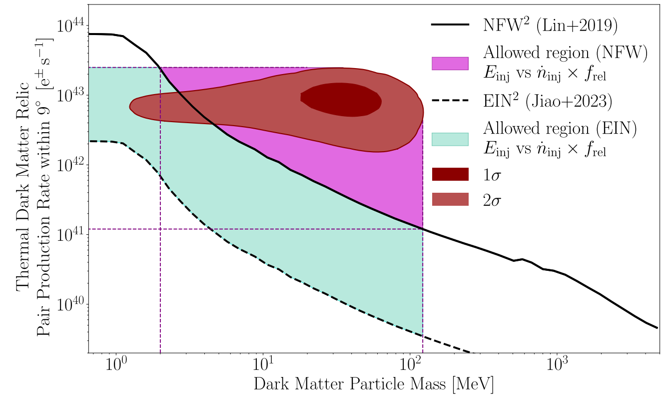

FIG. 3: Thermal relic dark matter annihilation rate versus particle mass. The black solid (cusped) and dashed (cored) lines show the maximum pair production rate from thermal relic dark matter for different halo models, while contours show 1 and 2σ confidence constraints from our fit to the 9° ROI. The allowed parameter space regions are shown in magenta and green, respectively.

that yields the lowest upper bound on $E_{\rm inj}$ is if we assume that the positrons cool in neutral rather than ionized gas, which yields $E_{\rm inj} < 37$ MeV (95% confidence).

DISCUSSION

Our results reveal a significant region of parameter space for positron injection at relativistic energies $\sim 40 - 60$ MeV, which is a significant relaxation compared to previous limits of a few MeV [55, 56]. This relaxation is a result of several important advances in both data and analysis. With regard to data, previous analyses implicitly assumed that the positron annihilation line is emitted solely from the Galactic bulge, while the continuum above the line comes from both the disk and the bulge, implying that the mechanism that makes the line must produce little to no continuum. However, recent studies [10] have shown that a significant fraction of the annihilation flux originates in the disk, and thus that the morphologies of the line and the continuum are much less well-separated than previously assumed. Second, unlike in previous analyses, we use a multi-component model of positron injection that includes a component from radionuclide decay, meaning only a fraction of the annihilation positrons are injected at relativistic energies. This is expected to relax the upper bounds. Finally, our calculation of the cooling radiation with CRIPTIC uses significantly more recent and accurate treatments of bremsstrahlung, Coulomb, and ionization losses, which cumulatively have the effect of reducing the predicted strength of cooling radiation compared to earlier work, leaving more room for higher-energy injection.

To further explore the implications of our results for the thermal relic dark matter scenario [59], in Figure 3 we show the region of dark matter particle mass ($m_\chi = E_{\rm inj}$) versus annihilation rate ($\dot{n}_{\rm ann} = f_{\rm rel}\dot{n}_{\rm e^+}$) allowed by our fit, with the limits extended to lower values in both parameters since as we have argued we should interpret our results as providing only an upper limit on these quantities. We overplot on this the expected dark matter annihilation rate for a thermal relic annihilation cross section assuming the Milky Way halo follows an NFW [75] (cusped; solid line) or Einasto [76] (cored; dashed line) profile; see End Matter for computational details. For the NFW case we see that our findings allow dark matter particle masses $\approx$ 2–120 MeV – the lower limit comes from the need to avoid producing too many positrons – while for the Einasto case we only find our ≈ 120 MeV upper limit. However, the fact that both the Einasto and NFW lines can pass well below the best-fit region implies that dark matter with a thermal relic cross section could account for at most 1–10% (NFW) or 0.1–10% (Einasto) of the γ-ray signal (or less if the annihilation branching ratio to e^+/e^- pairs is less than unity), with the balance having to come from another source of relativistic leptons. This finding suggests pulsars and cosmic rays as viable candidates for positron production, since these are expected to produce around 10^{42} e$^+$ s^{-1} in the bulge at tens of MeV [6].

The authors gratefully acknowledge useful communications with Celine Boehm, and thank Ranjan Laha for helpful comments on the manuscript. This research was undertaken with the assistance of resources from the National Computational Infrastructure (NCI Australia), an

NCRIS enabled capability supported by the Australian Government, through award jh2. SD's visit was supported by the Future Research Talent award from the Australian National University. LE is supported by the Bundesministerium für Wirtschaft und Klimaschutz via the Deutsches Zentrum für Luft- und Raumfahrt (DLR) under contract number 50 OR 2413 and is grateful for the support of the Studienstiftung des Deutschen Volkes.

* souradeeppdas@iisc.ac.in; soura2302@gmail.com
† Mark.Krumholz@anu.edu.au
‡ Roland.Crocker@anu.edu.au
§ thomas.siegert@uni-wuerzburg.de
¶ laura.eisenberger@uni-wuerzburg.de

[1] I. Johnson, W. N., J. Harnden, F. R., and R. C. Haymes, The Spectrum of Low-Energy Gamma Radiation from the Galactic-Center Region., ApJ **172**, L1 (1972).

[2] M. Leventhal, C. J. MacCallum, and P. D. Stang, Detection of 511 keV positron annihilation radiation from the galactic center direction., ApJ **225**, L11 (1978).

[3] W. R. Purcell, L. X. Cheng, D. D. Dixon, R. L. Kinzer, J. D. Kurfess, M. Leventhal, M. A. Saunders, J. G. Skibo, D. M. Smith, and J. Tueller, OSSE Mapping of Galactic 511 keV Positron Annihilation Line Emission, ApJ **491**, 725 (1997).

[4] R. L. Kinzer, P. A. Milne, J. D. Kurfess, M. S. Strickman, W. N. Johnson, and W. R. Purcell, Positron Annihilation Radiation from the Inner Galaxy, ApJ **559**, 282 (2001).

[5] R. Diehl, N. Prantzos, and P. von Ballmoos, Astrophysical constraints from gamma-ray spectroscopy, Nucl. Phys. A **777**, 70 (2006), arXiv:astro-ph/0502324 [astro-ph].

[6] N. Prantzos, C. Boehm, A. M. Bykov, R. Diehl, K. Ferrière, N. Guessoum, P. Jean, J. Knoedlseder, A. Marcowith, I. V. Moskalenko, A. Strong, and G. Weidenspointner, The 511 keV emission from positron annihilation in the Galaxy, Reviews of Modern Physics **83**, 1001 (2011), arXiv:1009.4620 [astro-ph.HE].

[7] C. Kierans, J. F. Beacom, S. Boggs, M. Buckley, R. Caputo, R. Crocker, M. De Becker, R. Diehl, C. L. Fryer, S. Griffin, D. Hartmann, E. Hays, P. Jean, M. G. H. Krause, T. Linden, A. Marcowith, P. Martin, A. Moiseev, U. Oberlack, E. Orlando, F. Panther, N. Prantzos, R. Rothschild, I. Seitenzahl, C. Shrader, T. Siegert, A. Strong, J. Tomsick, W. T. Vestrand, and A. Zoglauer, Positron Annihilation in the Galaxy, BAAS **51**, 256 (2019), arXiv:1903.05569 [astro-ph.HE].

[8] T. Siegert, The Positron Puzzle, Ap&SS **368**, 27 (2023), arXiv:2303.15582 [astro-ph.HE].

[9] F. A. Aharonian and A. M. Atoyan, On the Origin of the Galactic Annihilation Radiation, Soviet Astronomy Letters **7**, 395 (1981).

[10] T. Siegert, R. Diehl, G. Khachatryan, M. G. H. Krause, F. Guglielmetti, J. Greiner, A. W. Strong, and X. Zhang, Gamma-ray spectroscopy of positron annihilation in the Milky Way, A&A **586**, A84 (2016), arXiv:1512.00325 [astro-ph.HE].

[11] K.-W. Chan and R. E. Lingenfelter, Positrons from Supernovae, ApJ **405**, 614 (1993).

[12] J. Knödlseder, V. Lonjou, P. Jean, M. Allain, P. Mandrou, J. P. Roques, G. K. Skinner, G. Vedrenne, P. von Ballmoos, G. Weidenspointner, P. Caraveo, B. Cordier, V. Schönfelder, and B. J. Teegarden, Early SPI/INTEGRAL constraints on the morphology of the 511 keV line emission in the 4th galactic quadrant, A&A **411**, L457 (2003), arXiv:astro-ph/0309442 [astro-ph].

[13] J. Knödlseder, P. Jean, V. Lonjou, G. Weidenspointner, N. Guessoum, W. Gillard, G. Skinner, P. von Ballmoos, G. Vedrenne, J. P. Roques, S. Schanne, B. Teegarden, V. Schönfelder, and C. Winkler, The all-sky distribution of 511 keV electron-positron annihilation emission, A&A **441**, 513 (2005), arXiv:astro-ph/0506026 [astro-ph].

[14] G. Weidenspointner, C. R. Shrader, J. Knödlseder, P. Jean, V. Lonjou, N. Guessoum, R. Diehl, W. Gillard, M. J. Harris, G. K. Skinner, P. von Ballmoos, G. Vedrenne, J. P. Roques, S. Schanne, P. Sizun, B. J. Teegarden, V. Schönfelder, and C. Winkler, The sky distribution of positronium annihilation continuum emission measured with SPI/INTEGRAL, A&A **450**, 1013 (2006), arXiv:astro-ph/0601673 [astro-ph].

[15] N. Prantzos, On the intensity and spatial morphology of the 511 keV emission in the Milky Way, A&A **449**, 869 (2006), arXiv:astro-ph/0511190 [astro-ph].

[16] L. Bouchet, J. P. Roques, and E. Jourdain, On the Morphology of the Electron-Positron Annihilation Emission as Seen by Spi/integral, ApJ **720**, 1772 (2010), arXiv:1007.4753 [astro-ph.HE].

[17] R. M. Crocker, A. J. Ruiter, I. R. Seitenzahl, F. H. Panther, S. Sim, H. Baumgardt, A. Möller, D. M. Nataf, L. Ferrario, J. J. Eldridge, M. White, B. E. Tucker, and F. Aharonian, Diffuse Galactic antimatter from faint thermonuclear supernovae in old stellar populations, Nature Astronomy **1**, 0135 (2017), arXiv:1607.03495 [astro-ph.HE].

[18] T. B. Mera Evans, P. Hoeflich, and R. Diehl, Galactic Positrons from Thermonuclear Supernovae, ApJ **930**, 107 (2022), arXiv:2202.05417 [astro-ph.HE].

[19] P. Jean, W. Gillard, A. Marcowith, and K. Ferrière, Positron transport in the interstellar medium, A&A **508**, 1099 (2009), arXiv:0909.4022 [astro-ph.HE].

[20] J. C. Higdon, R. E. Lingenfelter, and R. E. Rothschild, The Galactic Positron Annihilation Radiation and the Propagation of Positrons in the Interstellar Medium, ApJ **698**, 350 (2009), arXiv:0711.3008 [astro-ph].

[21] R. E. Lingenfelter, J. C. Higdon, and R. E. Rothschild, Is There a Dark Matter Signal in the Galactic Positron Annihilation Radiation?, Phys. Rev. Lett. **103**, 031301 (2009), arXiv:0904.1025 [astro-ph.HE].

[22] F. H. Panther, Positron Transport and Annihilation in the Galactic Bulge, Galaxies **6**, 39 (2018), arXiv:1801.09365 [astro-ph.HE].

[23] T. Siegert, R. M. Crocker, O. Macias, F. H. Panther, F. Calore, D. Song, and S. Horiuchi, Measuring the smearing of the Galactic 511-keV signal: positron propagation or supernova kicks?, MNRAS **509**, L11 (2022), arXiv:2109.03691 [astro-ph.HE].

[24] P. De la Torre Luque, S. Balaji, and J. Koechler, Importance of Cosmic-Ray Propagation on Sub-GeV Dark Matter Constraints, ApJ **968**, 46 (2024), arXiv:2311.04979 [hep-ph].

[25] W. Wang, C. S. J. Pun, and K. S. Cheng, Could electron-positron annihilation lines in the Galactic center result from pulsar winds?, A&A **446**, 943 (2006), arXiv:astro-

ph/0509760 [astro-ph].
[26] S. Heinz and R. Sunyaev, Cosmic rays from microquasars: A narrow component to the CR spectrum?, A&A **390**, 751 (2002), arXiv:astro-ph/0204183 [astro-ph].
[27] N. Guessoum, P. Jean, and N. Prantzos, Microquasars as sources of positron annihilation radiation, A&A **457**, 753 (2006), arXiv:astro-ph/0607296 [astro-ph].
[28] T. Siegert, R. Diehl, J. Greiner, M. G. H. Krause, A. M. Beloborodov, M. C. Bel, F. Guglielmetti, J. Rodriguez, A. W. Strong, and X. Zhang, Positron annihilation signatures associated with the outburst of the microquasar V404 Cygni, Nature **531**, 341 (2016), arXiv:1603.01169 [astro-ph.HE].
[29] G. Weidenspointner, G. Skinner, P. Jean, J. Knödlseder, P. von Ballmoos, G. Bignami, R. Diehl, A. W. Strong, B. Cordier, S. Schanne, and C. Winkler, An asymmetric distribution of positrons in the Galactic disk revealed by γ-rays, Nature **451**, 159 (2008).
[30] G. Weidenspointner, G. K. Skinner, P. Jean, J. Knödlseder, P. von Ballmoos, R. Diehl, A. Strong, B. Cordier, S. Schanne, and C. Winkler, Positron astronomy with SPI/INTEGRAL, New A Rev. **52**, 454 (2008).
[31] R. Bartels, F. Calore, E. Storm, and C. Weniger, Galactic binaries can explain the Fermi Galactic centre excess and 511 keV emission, MNRAS **480**, 3826 (2018), arXiv:1803.04370 [astro-ph.HE].
[32] G. M. Fuller, A. Kusenko, D. Radice, and V. Takhistov, Positrons and 511 keV Radiation as Tracers of Recent Binary Neutron Star Mergers, Phys. Rev. Lett. **122**, 121101 (2019), arXiv:1811.00133 [astro-ph.HE].
[33] C. Boehm, D. Hooper, J. Silk, M. Casse, and J. Paul, MeV Dark Matter: Has It Been Detected?, Phys. Rev. Lett. **92**, 101301 (2004), arXiv:astro-ph/0309686 [astro-ph].
[34] D. Hooper and L.-T. Wang, Possible evidence for axino dark matter in the galactic bulge, Phys. Rev. D **70**, 063506 (2004), arXiv:hep-ph/0402220 [astro-ph].
[35] Y. Ascasibar, P. Jean, C. Bœhm, and J. Knödlseder, Constraints on dark matter and the shape of the Milky Way dark halo from the 511-keV line, MNRAS **368**, 1695 (2006), arXiv:astro-ph/0507142 [astro-ph].
[36] M. Pospelov and A. Ritz, The galactic 511 keV line from electroweak scale WIMPs, Physics Letters B **651**, 208 (2007), arXiv:hep-ph/0703128 [hep-ph].
[37] N. Arkani-Hamed, D. P. Finkbeiner, T. R. Slatyer, and N. Weiner, A theory of dark matter, Phys. Rev. D **79**, 015014 (2009), arXiv:0810.0713 [hep-ph].
[38] A. C. Vincent, P. Martin, and J. M. Cline, Interacting dark matter contribution to the galactic 511 keV gamma ray emission: constraining the morphology with INTEGRAL/SPI observations, J. Cosmology Astropart. Phys. **2012**, 022 (2012), arXiv:1201.0997 [hep-ph].
[39] Y. Ema, F. Sala, and R. Sato, Dark matter models for the 511 keV galactic line predict keV electron recoils on Earth, European Physical Journal C **81**, 129 (2021), arXiv:2007.09105 [hep-ph].
[40] P. De la Torre Luque, S. Balaji, and J. Silk, New 511 keV line data provides strongest sub-GeV dark matter constraints, arXiv e-prints , arXiv:2312.04907 (2023), arXiv:2312.04907 [hep-ph].
[41] D. P. Finkbeiner and N. Weiner, Exciting dark matter and the INTEGRAL/SPI 511keV signal, Phys. Rev. D **76**, 083519 (2007), arXiv:astro-ph/0702587 [astro-ph].
[42] D. P. Finkbeiner, T. R. Slatyer, N. Weiner, and I. Yavin, PAMELA, DAMA, INTEGRAL and signatures of metastable excited WIMPs, J. Cosmology Astropart. Phys. **2009**, 037 (2009), arXiv:0903.1037 [hep-ph].
[43] F. Chen, J. M. Cline, and A. R. Frey, New twist on excited dark matter: Implications for INTEGRAL, PAMELA/ATIC/PPB-BETS, DAMA, Phys. Rev. D **79**, 063530 (2009), arXiv:0901.4327 [hep-ph].
[44] F. Chen, J. M. Cline, A. Fradette, A. R. Frey, and C. Rabideau, Exciting dark matter in the Galactic Center, Phys. Rev. D **81**, 043523 (2010), arXiv:0911.2222 [hep-ph].
[45] J. M. Cline, A. R. Frey, and F. Chen, Metastable dark matter mechanisms for INTEGRAL 511 keV γ rays and DAMA/CoGeNT events, Phys. Rev. D **83**, 083511 (2011), arXiv:1008.1784 [hep-ph].
[46] J. M. Cline and A. R. Frey, Abelian dark matter models for 511 keV γ rays and direct detection, Annalen der Physik **524**, 579 (2012), arXiv:1204.1965 [hep-ph].
[47] C. V. Cappiello, M. Jafs, and A. C. Vincent, The morphology of exciting dark matter and the galactic 511 keV signal, J. Cosmology Astropart. Phys. **2023**, 003 (2023), arXiv:2307.15114 [hep-ph].
[48] R. Laha, Primordial Black Holes as a Dark Matter Candidate Are Severely Constrained by the Galactic Center 511 keV γ -Ray Line, Phys. Rev. Lett. **123**, 251101 (2019), arXiv:1906.09994 [astro-ph.HE].
[49] W. DeRocco and P. W. Graham, Constraining Primordial Black Hole Abundance with the Galactic 511 keV Line, Phys. Rev. Lett. **123**, 251102 (2019), arXiv:1906.07740 [astro-ph.CO].
[50] B. Dasgupta, R. Laha, and A. Ray, Neutrino and Positron Constraints on Spinning Primordial Black Hole Dark Matter, Phys. Rev. Lett. **125**, 101101 (2020), arXiv:1912.01014 [hep-ph].
[51] C. Keith and D. Hooper, 511 keV excess and primordial black holes, Phys. Rev. D **104**, 063033 (2021), arXiv:2103.08611 [astro-ph.CO].
[52] P. De la Torre Luque, J. Koechler, and S. Balaji, Refining Galactic primordial black hole evaporation constraints, arXiv e-prints , arXiv:2406.11949 (2024), arXiv:2406.11949 [astro-ph.HE].
[53] R.-G. Cai, Y.-C. Ding, X.-Y. Yang, and Y.-F. Zhou, Constraints on a mixed model of dark matter particles and primordial black holes from the galactic 511 keV line, J. Cosmology Astropart. Phys. **2021**, 057 (2021), arXiv:2007.11804 [astro-ph.CO].
[54] P. De la Torre Luque, S. Balaji, M. Fairbairn, F. Sala, and J. Silk, 511 keV Galactic Photons from a Dark Matter Spike, arXiv e-prints , arXiv:2410.16379 (2024), arXiv:2410.16379 [astro-ph.HE].
[55] J. F. Beacom and H. Yüksel, Stringent Constraint on Galactic Positron Production, Phys. Rev. Lett. **97**, 071102 (2006), arXiv:astro-ph/0512411 [astro-ph].
[56] P. Sizun, M. Cassé, and S. Schanne, Continuum γ-ray emission from light dark matter positrons and electrons, Phys. Rev. D **74**, 063514 (2006), arXiv:astro-ph/0607374 [astro-ph].
[57] P. Sizun, M. Cassé, S. Schanne, and B. Cordier, Constraints on the Injection Energy of Positrons in the Galactic Centre Region, in *The Obscured Universe. Proceedings of the VI INTEGRAL Workshop*, ESA Special Publication, Vol. 622 (2007) p. 61, arXiv:astro-ph/0702061 [astro-ph].

[58] M. Pospelov, A. Ritz, and M. Voloshin, Secluded WIMP dark matter, Physics Letters B **662**, 53 (2008), arXiv:0711.4866 [hep-ph].

[59] T. R. Slatyer, Indirect dark matter signatures in the cosmic dark ages. I. Generalizing the bound on s -wave dark matter annihilation from Planck results, Phys. Rev. D **93**, 023527 (2016), arXiv:1506.03811 [hep-ph].

[60] M. R. Krumholz, R. M. Crocker, and M. L. Sampson, Cosmic ray interstellar propagation tool using Itô Calculus (CRIPTIC): software for simultaneous calculation of cosmic ray transport and observational signatures, MNRAS **517**, 1355 (2022), arXiv:2207.13838 [astro-ph.HE].

[61] R. Diehl, T. Siegert, J. Greiner, M. Krause, K. Kretschmer, M. Lang, M. Pleintinger, A. W. Strong, C. Weinberger, and X. Zhang, INTEGRAL/SPI γ-ray line spectroscopy. Response and background characteristics, A&A **611**, A12 (2018), arXiv:1710.10139 [astro-ph.IM].

[62] T. Siegert, J. Berteaud, F. Calore, P. D. Serpico, and C. Weinberger, Diffuse Galactic emission spectrum between 0.5 and 8.0 MeV, A&A **660**, A130 (2022), arXiv:2202.04574 [astro-ph.HE].

[63] E. Churazov, S. Sazonov, S. Tsygankov, R. Sunyaev, and D. Varshalovich, Positron annihilation spectrum from the Galactic Centre region observed by SPI/INTEGRAL revisited: annihilation in a cooling ISM?, MNRAS **411**, 1727 (2011), arXiv:1010.0864 [astro-ph.HE].

[64] A. W. Strong, H. Bloemen, R. Diehl, W. Hermsen, and V. Schönfelder, COMPTEL Skymapping: a New Approach Using Parallel Computing, Astrophysical Letters and Communications **39**, 209 (1999), arXiv:astro-ph/9811211 [astro-ph].

[65] J. F. Beacom, N. F. Bell, and G. Bertone, Gamma-Ray Constraint on Galactic Positron Production by MeV Dark Matter, Phys. Rev. Lett. **94**, 171301 (2005), arXiv:astro-ph/0409403 [astro-ph].

[66] C. Boehm and P. Uwer, Revisiting Bremsstrahlung emission associated with Light Dark Matter annihilations, arXiv e-prints , hep-ph/0606058 (2006), arXiv:hep-ph/0606058 [hep-ph].

[67] P. Martin, A. W. Strong, P. Jean, A. Alexis, and R. Diehl, Galactic annihilation emission from nucleosynthesis positrons, A&A **543**, A3 (2012), arXiv:1205.1194 [astro-ph.HE].

[68] N. Guessoum, P. Jean, and W. Gillard, The lives and deaths of positrons in the interstellar medium, A&A **436**, 171 (2005), arXiv:astro-ph/0504186 [astro-ph].

[69] A. Ore and J. L. Powell, Three-photon annihilation of an electron-positron pair, Phys. Rev. **75**, 1696 (1949).

[70] R. Krivonos, M. Revnivtsev, E. Churazov, S. Sazonov, S. Grebenev, and R. Sunyaev, Hard X-ray emission from the Galactic ridge, A&A **463**, 957 (2007), arXiv:astro-ph/0605420 [astro-ph].

[71] A. Lutovinov, V. Suleimanov, G. J. Manuel Luna, S. Sazonov, D. de Martino, L. Ducci, V. Doroshenko, and M. Falanga, INTEGRAL View on cataclysmic variables and symbiotic binaries, New A Rev. **91**, 101547 (2020), arXiv:2008.10665 [astro-ph.HE].

[72] J. Berteaud, F. Calore, J. Iguaz, P. D. Serpico, and T. Siegert, Strong constraints on primordial black hole dark matter from 16 years of INTEGRAL/SPI observations, Phys. Rev. D **106**, 023030 (2022), arXiv:2202.07483 [astro-ph.HE].

[73] F. Calore, A. Dekker, P. D. Serpico, and T. Siegert, Constraints on light decaying dark matter candidates from 16 yr of INTEGRAL/SPI observations, MNRAS **520**, 4167 (2023), arXiv:2209.06299 [hep-ph].

[74] T. Siegert, Galactic Diffuse Emission Spectrum between 0.5 and 8.0 MeV and between 30 keV and 8 MeV for the search of PBH Dark Matter, 10.5281/zenodo.6505275 (2021).

[75] H.-N. Lin and X. Li, The dark matter profiles in the Milky Way, MNRAS **487**, 5679 (2019), arXiv:1906.08419 [astro-ph.GA].

[76] Y. Jiao, F. Hammer, H. Wang, J. Wang, P. Amram, L. Chemin, and Y. Yang, Detection of the Keplerian decline in the Milky Way rotation curve, A&A **678**, A208 (2023), arXiv:2309.00048 [astro-ph.GA].

[77] V. Zabalza, Naima: a Python package for inference of particle distribution properties from nonthermal spectra, in *34th International Cosmic Ray Conference (ICRC2015)*, International Cosmic Ray Conference, Vol. 34 (2015) p. 922, arXiv:1509.03319 [astro-ph.HE].

[78] D. Khangulyan, F. A. Aharonian, and S. R. Kelner, Simple Analytical Approximations for Treatment of Inverse Compton Scattering of Relativistic Electrons in the Blackbody Radiation Field, ApJ **783**, 100 (2014), arXiv:1310.7971 [astro-ph.HE].

[79] M. R. Krumholz, R. M. Crocker, and S. S. R. Offner, The cosmic ray ionization and γ-ray budgets of star-forming galaxies, MNRAS **520**, 5126 (2023), arXiv:2211.03488 [astro-ph.GA].

[80] Y.-K. Kim, J. P. Santos, and F. Parente, Extension of the binary-encounter-dipole model to relativistic incident electrons, Phys. Rev. A **62**, 052710 (2000).

[81] R. J. Gould, Energy loss of fast electrons and positrons in a plasma, Physica **60**, 145 (1972).

[82] G. R. Blumenthal and R. J. Gould, Bremsstrahlung, Synchrotron Radiation, and Compton Scattering of High-Energy Electrons Traversing Dilute Gases, Reviews of Modern Physics **42**, 237 (1970).

[83] D. Foreman-Mackey, D. W. Hogg, D. Lang, and J. Goodman, emcee: The MCMC Hammer, PASP **125**, 306 (2013), arXiv:1202.3665 [astro-ph.IM].

[84] M. Kamionkowski, S. M. Koushiappas, and M. Kuhlen, Galactic substructure and dark-matter annihilation in the Milky Way halo, Phys. Rev. D **81**, 043532 (2010), arXiv:1001.3144 [astro-ph.GA].

END MATTER

Background Emission Model

Our model for the background to the lepton emission includes two components. The first is a population of unresolved point sources, whose spectral contribution we model as a power-law with an upper cutoff at 511 keV with functional form $d\dot{n}_\gamma^{\rm UPS}/dE_\gamma = (\mathcal{N}_{\rm UPS}/E_\gamma)(E_\gamma/E_0)^{\alpha_{\rm UPS}}$, where $E_0 = 50$ keV, and $\mathcal{N}_{\rm UPS}$ and $\alpha_{\rm UPS}$ are free parameters. The second is inverse Compton (IC) emission from a population of electrons produced dominantly by conventional shock acceleration, which we parameterize with an energy distribution $dn_e/dE_e \propto E_e^p$ for $E_e > 1$ GeV, where the slope p is a free parameter. These interact with a background radiation field consisting of three components with blackbody spectral shapes: the cosmic microwave background ($T = 2.73$ K), a far-infrared (FIR) dust radiation ($T = 30$ K), and near-infrared (NIR) starlight ($T = 3000$ K). We compute the spectral shape of the resulting IC emission using the `naima` package [77, 78], and we normalize this emission by setting the IC luminosity per unit energy at photon energy $E_\gamma = 511$ keV to a value $\mathcal{N}_{\rm CMB}$; this value implicitly fixes the normalization of the electron spectrum. We then normalize the IC contribution from the NIR and FIR components by defining $x_{\rm NIR}$ and $x_{\rm FIR}$ as the ratio of the energy densities in these two fields to those in the Solar neighborhood, $u_{\rm NIR} = 1$ eV cm^{-3} and $u_{\rm FIR} = 0.5$ eV cm^{-3}, respectively. We leave $\mathcal{N}_{\rm CMB}$, $x_{\rm NIR}$, and $x_{\rm FIR}$ as parameters to be fit, which together fully specify the IC spectrum $d\dot{n}_\gamma^{\rm IC}/dE_\gamma$.

ISM Cooling Radiation

We calculate the γ-ray emission rates $\mathrm{d}\dot{n}_\gamma^{\rm cool,e^\pm}/\mathrm{d}E_\gamma$ per injected cosmic ray from ISM cooling numerically from a series of simulations using the cosmic ray propagation code CRIPTIC [60], following the approach in ref. [79]; CRIPTIC's advantages include that it provides a fully probabilistic treatment of bremsstrahlung and inverse Compton that allows realistic catastrophic losses rather than using the continuous slowing-down approximation (CSDA) and that it uses modern estimates for reaction cross sections and radiative emission. In particular, its treatment of ionization losses uses the relativistic BEQ formalism of ref. [80], Coulomb losses uses the formalism of ref. [81], and the treatment of bremsstrahlung (including nuclear shielding) is taken from ref. [82]. In contrast, some earlier work relied on approximate analytic fitting formulae and the CSDA for these processes.

In each simulation we inject an initially mono-energetic population of electrons/positrons into a medium in which the helium abundance per H nucleon is 0.0955, and the hydrogen is assumed to be either 99% atomic and 1% ionized or fully ionized (our fiducial choice). The medium has both a magnetic field and a radiation field that is described as a sum of three (dilute) blackbody components with temperatures of 2.73 K, 30 K, and 3000 K (corresponding roughly to the cosmic microwave background, the dust radiation field, and the starlight field), whose energy densities are in a ratio 1 : 1.19 : 2.34, roughly the ratio seen locally. Ref. [79] point out that the photon emission per injected particle $\mathrm{d}\dot{n}^{\rm cool,e^\pm}/\mathrm{d}E_\gamma$ does not depend on the absolute gas density or on the energy densities of the magnetic and radiation fields. Instead, it depends only on the chemical state of the gas, the shape of the background radiation spectrum, and on two dimensionless ratios $f_{\rm IC}$ and $f_{\rm sync}$ (their Equation 11), which specify the strength of inverse Compton and synchrotron losses relative to collisional losses. For our fiducial run we adopt $f_{\rm IC} \approx f_{\rm synch} \approx 10^{-6}$.

We run simulations at 241 initial kinetic energies T_i each for both electrons and positrons; the first 201 sample points are uniformly distributed in logarithm from 100 keV to 10 MeV, and the remaining 40 points extend the grid up to 1 GeV, again with uniform logarithmic spacing from 10 MeV to 1 GeV. In each simulation particles with energy T_i are injected at a steady rate, and we follow them until their kinetic energies drop below 1 keV, at which point their energies are low enough that we can treat them as thermalized. Following ref. [79], we use a packet injection rate $\Gamma = 2 \times 10^{-9}(n_{\rm H}/\mathrm{cm}^{-3})$ s^{-1}, where $n_{\rm H}$ is the background number density of H nuclei, a step size control parameter $c_{\rm step} = 0.05$, and a secondary production factor $f_{\rm sec} = 0.1$. We initially run the simulations until the time reaches $5 \times (10^9, 10^{10})/(n_{\rm H}/\mathrm{cm}^{-3})$ s for $(T_i < 100, T_i \geq 100)$ MeV, at least five times the time required for the system to settle into steady state between particle injection and cooling.

After this point we continue the simulations to a time $3 \times (10^{10}, 10^{11})/(n_{\rm H}/\mathrm{cm}^{-3})$ s, sampling the emission at 126 uniformly-spaced times, and take $\mathrm{d}\dot{n}^{\rm cool,e^\pm}/\mathrm{d}E_\gamma$ for that value of T_i to be the average of the instantaneous emission rates predicted at these times. We similarly measure $f_{\rm IFA}$, the fraction of positrons that undergo in-flight annihilation, from the difference between the positron injection rate and the rate at which positrons cool to $T < 1$ keV and we stop following them. This process therefore yields measurements of $\mathrm{d}\dot{n}^{\rm cool,e^\pm}/\mathrm{d}E_\gamma$ and $f_{\rm IFA}$ at our 241 sample values of T_i. For the purposes of calculating these quantities in the rest of our analysis, we simply interpolate on these tables.

Our fiducial choice of ionized composition and $f_{\rm sync} \approx f_{\rm IC} \approx 10^{-6}$ are reasonable and realistic parameters for the ISM in which positrons cool, but other choices are certainly possible. To evaluate the impact of these choices, we carry out a systematic study in which we recalculate the cooling rate using the same method but for alternative choices, and then repeat our full analysis

Parameter	Unit	Prior
$\log \dot{n}_{e^+}^{\rm inj}/4\pi D^2$	$\rm cm^{-2}\ s^{-1}$	$\mathcal{U}(-5.0, -2.0)$
$\log E_{\rm inj}$	keV	$\mathcal{U}(3.0, \log_{10}(3\times 10^5))$
$f_{\rm rel}$, f_β, $f_{^{26}\rm Al}$	-	$\rm Dir(1,1,1)$
$f_{\rm Ps}$	-	$\mathcal{U}(0.9, 1.0)$
$\log \mathcal{N}_{\rm CMB}/4\pi D^2$	$\rm cm^{-2}\ s^{-1}$	$\mathcal{U}(-10.0, 0.0)$
$\log x_{\rm FIR}$	-	$\mathcal{U}(-3.0, 5.0)$
$\log x_{\rm NIR}$	-	$\mathcal{U}(-3.0, 5.0)$
p	-	$\mathcal{U}(-3.0, -2.0)$
$\log \mathcal{N}_{\rm UPS}/4\pi D^2$	$\rm cm^{-2}\ s^{-1}$	$\mathcal{U}(-4.0, 0.0)$
$\theta_{\rm UPS} = \tan^{-1}\alpha_{\rm UPS}$	-	$\mathcal{U}(-\pi/2, 0)$

TABLE A1: Model parameters, units, and priors. Here $\mathcal{U}(a,b)$ is the uniform distribution from a to b and $\rm Dir(1,1,1)$ is the flat Dirichlet distribution; note that, because $f_{\rm rel}$, f_β, and $f_{^{26}\rm Al}$ are drawn from this distribution, and thus their sum is constrained to unity, only two of these parameters are free.

pipeline using these alternative choices. We summarize the full set of parameters we have tested, and provide results derived from them, in Table S2 of the Supplemental Material. As discussed in the main text, the results change little as we vary these parameters within reasonable limits, with the largest effects resulting from changing between atomic and ionized composition because Coulomb losses are slightly more efficient than ionization losses and thus an atomic medium directs somewhat more of the cooling into detectable radiation rather than invisible collisions.

Fitting Method

Our model has 11 free parameters. The leptonic emission is parametrized by: the total injection rate of positrons $\dot{n}_{e^+}^{\rm inj}/4\pi D^2$ normalized by the effective source distance D, the injection energy $E_{\rm inj}$, the fraction $f_{\rm rel}$ of positrons injected by relativistic sources, the fraction f_β injected by β^+-decay of nuclei other than ^{26}Al (from which one derives the ^{26}Al fraction $f_{^{26}\rm Al} = 1 - f_{\rm rel} - f_\beta$), and the positronium fraction $f_{\rm Ps}$ (known to be close to 100% [10]). Parameters for the background emission are: the normalization $\mathcal{N}_{\rm CMB}/4\pi D^2$ of IC background from up-scattered CMB, the ratios $x_{\rm FIR}$ and $x_{\rm NIR}$, respectively, of the FIR and NIR radiation energy densities to that in the solar neighbourhood, the slope p (known to be ≈ -3 to -2) of the cosmic ray electron energy distribution at energies ≥ 1 GeV, and the normalization $\mathcal{N}_{\rm UPS}/4\pi D^2$ and slope $\alpha_{\rm UPS}$ of the UPS background component.

In order to estimate constraints on the parameters, we use a Bayesian parameter inference method using the Markov-Chain Monte Carlo (MCMC) sampler `emcee` [83]. For the purposes of this calculation we adopt the priors listed in Table A1. These are mostly flat (in logarithm) over a very large parameter range. The only exceptions are: (1) for the fraction $f_{\rm rel}$ and f_β, and the implicit corresponding parameter $f_{^{26}\rm Al}$, we adopt the 3d-flat Dirichlet distribution, appropriate for three parameters constrained to have a fixed sum; (2) for $f_{\rm Ps}$ and p we use tight priors that are uniform from 0.9 to 1 and -3 to -2, since these quantities are known from other constraints; (3) for $\alpha_{\rm UPS}$, we use the standard Jeffreys prior for slopes, whereby the prior is uniform in the angle $\theta_{\rm UPS} = \tan^{-1}\alpha_{\rm UPS}$.

We run 104 MCMC chains for 60,000 burn-in steps followed by 200,000 production steps per chain, with an estimated autocorrelation time ≈ 2000. To identify which scaling model best describes each ROI, we compute the Akaike Information Criterion (AIC) for each of the fits (that is, for every scaling model in each of the ROIs):

$$\mathrm{AIC} = 2k - 2\log\mathcal{L}_{\rm max}, \tag{A1}$$

where $k = 11$ is the number of degrees of freedom of the model and $\mathcal{L}_{\rm max}$ is the maximum of the likelihood function as found by our MCMC. We compare the scaling models in each ROI using the Bayes factor

$$f_{\rm Bayes,i} = \frac{\exp(-\mathrm{AIC}_i/2)}{\sum_j \exp(-\mathrm{AIC}_j/2)}, \tag{A2}$$

where i and j run over the three scaling models for each ROI. We accept the model with the highest Bayes factor in each ROI (for example, `ptsrc` in the 9° region) as the most plausible scaling to adopt when combining the INTEGRAL and CGRO data. Examining the chosen fits, these tend to be the scalings that yield the smoothest transition between the lower-energy INTEGRAL data and the higher-energy CGRO bands, while scaling choices that lead to a noticeable jump between the two are disfavored.

Thermal Relic Dark Matter Pair Production

We calculate the electron-positron pair production rate from thermal relic dark matter as

$$\Gamma_{\rm ee} = \frac{1}{2} L(\Delta\Omega)\, \langle\sigma(m_\chi)v(m_\chi)\rangle\, m_\chi^{-2}, \tag{A3}$$

where m_χ is the dark matter particle mass, $\langle\sigma(m_\chi)v(m_\chi)\rangle$ is the velocity-averaged thermal relic cross section [59], and $L(\Delta\Omega)$ is the luminosity of a dark matter halo that is self-annihilating, given by

$$L(\Delta\Omega) = \iint_{\Delta\Omega} d\Omega \int_0^{+\infty} ds\, s^2\, \rho^2(s,\ell,b). \tag{A4}$$

This formalism explicitly assumes that 100% of the dark matter annihilations go into pairs. If other channels are allowed, such as to $\nu\bar{\nu}$ or $\gamma\gamma$, which is always the case for $m_\chi \lesssim m_\mu$, the pair production rate could in fact be even smaller. We do not include a boost factor because boosts only become important in the outskirts of a galaxy beyond $\sim 20\,\mathrm{kpc}$ [84], well beyond our observed region.

Relaxation of Energy Constraints for Positrons Generating the Galactic Annihilation Signal

Supplemental Material

Souradeep Das, Mark R. Krumholz, Roland M. Crocker, Thomas Siegert, and Laura Eisenberger

EMISSION FROM COOLING POSITRONS

As discussed in the main text, the cooling radiation from positrons includes contributions from Bremsstrahlung (B), Inverse Compton (IC) and In-flight Annihilation (IFA). For electrons, only B and IC contribute to the cooling radiation. In our analysis, we calculate these components using the code CRIPTIC and present the spectral fit in Figure 2 of the main paper. In Figure S1 we present a breakup of these emission channels for relativistic positrons injected into the ISM. Note that this emission is sub-dominant to the thermalized radiation when the injected positrons are mildly relativistic or non-relativistic.

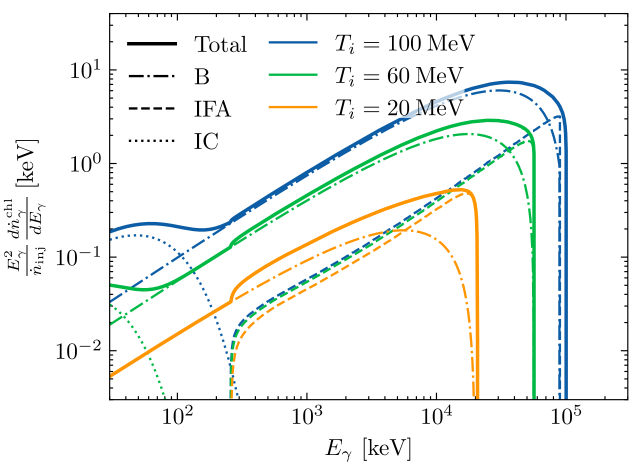

FIG. S1: γ-ray emission (normalized to the injection rate) from cooling positrons, computed using CRIPTIC, in our benchmark ISM model (See appendix of main paper), for 3 different injection energies. Thick, solid: Total cooling emission; dot-dashed: B; dashed: IFA; dotted: IC from injected positrons.

VARYING THE COMPOSITION AND DENSITY OF THE ISM

As discussed in the main text, the exact shape of the ISM photon production function $\mathrm{d}n_\gamma^{\mathrm{cool},e^\pm}/\mathrm{d}E_\gamma$ depends on the chemical state of the ISM (predominantly ionized versus atomic) and on the strengths of the interstellar magnetic and radiation fields, which in turn set the importance of synchrotron and inverse Compton losses to collisional losses, as parameterized by $f_{\rm sync}$ and $f_{\rm IC}$ [79]. These conditions in turn depend on where in the Galaxy the positrons propagate and annihilate.

In order to understand how varying these parameters would affect our final conclusion, we experimented with the following sets of ISM conditions:

- I: Ionized medium with $f_{\rm IC} = f_{\rm synch} = 10^{-5}$
- II: Ionized medium with $f_{\rm IC} = f_{\rm synch} = 10^{-6}$ (the benchmark model presented in the main text)
- III: Ionized medium with $f_{\rm IC} = f_{\rm synch} = 10^{-7}$
- IV: Ionized medium with $f_{\rm IC} = f_{\rm synch} = 10^{-8}$
- V: Atomic medium with $f_{\rm IC} = f_{\rm synch} = 10^{-6}$

In the full tables and figures below we present results for each of these ISM compositions, demonstrating that the qualitative conclusions do not change significantly between them.

COMPARING CGRO DATA SCALING MODELS

Again as discussed in the main text, we consider three models for how to scale the CGRO data relative to the INTEGRAL data for each ROI: `flat` , `like511` , and `ptsrc` . We choose between these models based on the Bayes factors calculated from Equations A1-A2 (of the main paper). In Table S1 we present the resulting Bayes factors, both for the Benchmark ISM model and the four alternatives described above. The results vary very little with ISM model; for all models we find that the `ptsrc` scaling yields the highest Bayes factor in small ROIs (5° and 9°), while the `flat` model performs the best in larger ROI's (18° and 95°).

POSTERIORS ON FULL MODEL PARAMETERS

In this section, we present the posteriors on the model parameters, obtained from MCMC analysis of the highest Bayes-factor scaling for each ROI, as described in End Matter of the main paper. These are reported for the fiducial ISM as well as alternative choices (see above). The posteriors for each of the cases are summarized in

ISM conditions	ROI	`flat`	`like511`	`ptsrc`
I. Ionized $f_{\mathrm{IC}} = 10^{-5}$	5°circle	0.1893	0.3175	**0.4932**
	9°circle	0.169	0.37	**0.461**
	18°circle	**0.9759**	0.0207	0.0034
	95°square	**1.0**	7.739×10^{-10}	4.445×10^{-13}
II. Ionized $f_{\mathrm{IC}} = 10^{-6}$ Benchmark model	5°circle	0.2563	0.2944	**0.4493**
	9°circle	0.1888	0.2967	**0.5146**
	18°circle	**0.9609**	0.0359	0.0032
	95°square	**1.0**	3.626×10^{-10}	2.069×10^{-13}
III. Ionized $f_{\mathrm{IC}} = 10^{-7}$	5°circle	0.197	0.3232	**0.4798**
	9°circle	0.2554	0.3372	**0.4074**
	18°circle	**0.9696**	0.0270	0.0034
	95°square	**1.0**	4.502×10^{-10}	2.13×10^{-13}
IV. Ionized $f_{\mathrm{IC}} = 10^{-8}$	5°circle	0.2204	0.3431	**0.4365**
	9°circle	0.2144	0.3209	**0.4647**
	18°circle	**0.9701**	0.0263	0.0036
	95°square	**1.0**	4.159×10^{-10}	2.039×10^{-13}
V. Atomic $f_{\mathrm{IC}} = 10^{-6}$	5°circle	0.3036	0.3321	**0.3643**
	9°circle	0.2339	0.3427	**0.4234**
	18°circle	**0.9072**	0.072	0.0208
	95°square	**1.0**	4.531×10^{-9}	1.358×10^{-11}

TABLE S1: Comparison of Bayes factors for each ROI under various ISM conditions

Table S2, the corresponding spectral fits in Figures S2-S6 (analogous to Figure 2 of the main paper), and the corner plots for all variables and all combinations of ROI and ISM model appear in Figures S7-S26.

	$\log_{10}\dot{n}^{\#}_{\rm inj}$	$E_{\rm inj}$/MeV	$f_{\rm rel}$	f_{β}	$f_{^{26}{\rm Al}}$	$f_{\rm Ps}$	$\log_{10}\mathcal{N}^{\#}_{\rm CMB}$	$\log_{10} x_{\rm FIR}$	$\log_{10} x_{\rm NIR}$	p	$\log_{10}\mathcal{N}^{\#}_{\rm UPS}$	$\alpha_{\rm UPS}$
ROI = 5°circle												
I	$-3.05^{+0.08}_{-0.10}$	$38.5^{+35.9}_{-36.8}$	$0.56^{+0.34}_{-0.46}$	$0.38^{+0.45}_{-0.34}$	$0.06^{+0.053}_{-0.044}$	$0.96^{+0.04}_{-0.05}$	$-7.60^{+3.55}_{-2.15}$	$0.51^{+3.79}_{-3.15}$	$0.36^{+3.90}_{-3.02}$	$-2.49^{+0.44}_{-0.46}$	$-2.8^{+0.39}_{-0.99}$	$-3.6^{+2.8}_{-4.7}$
II*	$-3.05^{+0.08}_{-0.10}$	$28^{+58.3}_{-26.4}$	$0.52^{+0.38}_{-0.46}$	$0.41^{+0.46}_{-0.38}$	$0.06^{+0.053}_{-0.045}$	$0.96^{+0.03}_{-0.05}$	$-7.49^{+3.53}_{-2.25}$	$0.52^{+3.82}_{-3.18}$	$0.33^{+3.94}_{-3.00}$	$-2.48^{+0.42}_{-0.47}$	$-2.6^{+0.3}_{-0.9}$	$-3.9^{+1.8}_{-5}$
III	$-3.05^{+0.08}_{-0.10}$	$27.4^{+57}_{-25.8}$	$0.52^{+0.38}_{-0.45}$	$0.41^{+0.45}_{-0.37}$	$0.059^{+0.054}_{-0.044}$	$0.96^{+0.03}_{-0.05}$	$-7.49^{+3.52}_{-2.25}$	$0.53^{+3.81}_{-3.17}$	$0.38^{+3.90}_{-3.04}$	$-2.49^{+0.44}_{-0.46}$	$-2.6^{+0.29}_{-0.85}$	$-3.8^{+1.8}_{-4.7}$
IV	$-3.04^{+0.08}_{-0.10}$	$27.6^{+59.5}_{-26}$	$0.53^{+0.37}_{-0.46}$	$0.41^{+0.46}_{-0.37}$	$0.058^{+0.054}_{-0.044}$	$0.96^{+0.03}_{-0.05}$	$-7.51^{+3.55}_{-2.21}$	$0.53^{+3.85}_{-3.16}$	$0.37^{+3.91}_{-3.04}$	$-2.48^{+0.43}_{-0.46}$	$-2.6^{+0.29}_{-0.89}$	$-3.8^{+1.8}_{-4.9}$
V	$-3.02^{+0.08}_{-0.10}$	$16.9^{+46.1}_{-15.3}$	$0.52^{+0.39}_{-0.46}$	$0.42^{+0.45}_{-0.38}$	$0.056^{+0.052}_{-0.042}$	$0.96^{+0.03}_{-0.05}$	$-7.47^{+3.51}_{-2.26}$	$0.47^{+3.86}_{-3.11}$	$0.37^{+3.88}_{-3.02}$	$-2.48^{+0.43}_{-0.47}$	$-2.6^{+0.29}_{-0.86}$	$-3.8^{+1.8}_{-4.8}$
ROI = 9°circle												
I	$-2.81^{+0.07}_{-0.09}$	$35.5^{+29.7}_{-32.1}$	$0.64^{+0.28}_{-0.47}$	$0.31^{+0.47}_{-0.28}$	$0.055^{+0.044}_{-0.038}$	$0.97^{+0.03}_{-0.06}$	$-7.04^{+3.55}_{-2.60}$	$1.08^{+3.50}_{-3.63}$	$0.01^{+4.01}_{-2.70}$	$-2.51^{+0.44}_{-0.43}$	$-2.4^{+0.29}_{-0.86}$	$-4^{+1.7}_{-4.6}$
II*	$-2.81^{+0.07}_{-0.09}$	$33^{+28.6}_{-30.6}$	$0.65^{+0.27}_{-0.51}$	$0.30^{+0.51}_{-0.27}$	$0.054^{+0.044}_{-0.037}$	$0.97^{+0.03}_{-0.06}$	$-6.90^{+3.49}_{-2.69}$	$1.15^{+3.44}_{-3.70}$	$-0.06^{+4.02}_{-2.65}$	$-2.51^{+0.44}_{-0.43}$	$-2.4^{+0.28}_{-0.86}$	$-4^{+1.6}_{-4.7}$
III	$-2.81^{+0.07}_{-0.09}$	$32.7^{+28.6}_{-30.2}$	$0.65^{+0.27}_{-0.51}$	$0.29^{+0.51}_{-0.27}$	$0.055^{+0.043}_{-0.038}$	$0.97^{+0.03}_{-0.06}$	$-6.95^{+3.50}_{-2.68}$	$1.20^{+3.41}_{-3.77}$	$-0.02^{+4.04}_{-2.67}$	$-2.51^{+0.44}_{-0.43}$	$-2.4^{+0.27}_{-0.76}$	$-4^{+1.6}_{-4.1}$
IV	$-2.81^{+0.07}_{-0.09}$	$33.1^{+28.8}_{-30.5}$	$0.64^{+0.28}_{-0.51}$	$0.30^{+0.50}_{-0.28}$	$0.055^{+0.043}_{-0.038}$	$0.97^{+0.03}_{-0.06}$	$-6.97^{+3.55}_{-2.65}$	$1.19^{+3.42}_{-3.74}$	$-0.07^{+4.00}_{-2.65}$	$-2.51^{+0.44}_{-0.43}$	$-2.4^{+0.27}_{-0.78}$	$-4^{+1.6}_{-4.3}$
V	$-2.78^{+0.08}_{-0.10}$	$18.1^{+19.1}_{-15.5}$	$0.70^{+0.23}_{-0.54}$	$0.25^{+0.54}_{-0.23}$	$0.05^{+0.042}_{-0.035}$	$0.97^{+0.03}_{-0.06}$	$-6.84^{+3.41}_{-2.75}$	$1.20^{+3.41}_{-3.75}$	$-0.05^{+4.06}_{-2.65}$	$-2.51^{+0.44}_{-0.43}$	$-2.4^{+0.27}_{-0.81}$	$-3.9^{+1.5}_{-4.4}$
ROI = 18°circle												
I	$-2.56^{+0.07}_{-0.08}$	$49.9^{+14.5}_{-29.3}$	$0.77^{+0.14}_{-0.36}$	$0.14^{+0.36}_{-0.13}$	$0.085^{+0.039}_{-0.035}$	$0.97^{+0.02}_{-0.06}$	$-6.23^{+3.17}_{-3.08}$	$1.95^{+2.76}_{-4.34}$	$-0.38^{+3.99}_{-2.34}$	$-2.51^{+0.39}_{-0.43}$	$-2.3^{+0.34}_{-1}$	$-4.3^{+2.3}_{-5.3}$
II*	$-2.57^{+0.07}_{-0.08}$	$45^{+16.1}_{-27.9}$	$0.77^{+0.14}_{-0.40}$	$0.14^{+0.40}_{-0.13}$	$0.085^{+0.04}_{-0.034}$	$0.97^{+0.02}_{-0.06}$	$-5.96^{+2.99}_{-2.95}$	$2.18^{+2.57}_{-4.49}$	$-0.40^{+3.87}_{-2.34}$	$-2.49^{+0.35}_{-0.43}$	$-2.2^{+0.31}_{-0.81}$	$-4.4^{+1.7}_{-4.4}$
III	$-2.57^{+0.07}_{-0.08}$	$44.6^{+16.2}_{-29}$	$0.77^{+0.14}_{-0.41}$	$0.14^{+0.40}_{-0.13}$	$0.085^{+0.04}_{-0.035}$	$0.97^{+0.02}_{-0.06}$	$-5.94^{+2.98}_{-3.01}$	$2.19^{+2.57}_{-4.51}$	$-0.45^{+3.97}_{-2.30}$	$-2.48^{+0.34}_{-0.43}$	$-2.2^{+0.31}_{-0.79}$	$-4.4^{+1.7}_{-4.3}$
IV	$-2.57^{+0.07}_{-0.08}$	$44.5^{+16.5}_{-27.6}$	$0.77^{+0.14}_{-0.42}$	$0.14^{+0.41}_{-0.13}$	$0.085^{+0.04}_{-0.035}$	$0.97^{+0.03}_{-0.06}$	$-5.94^{+2.98}_{-2.95}$	$2.19^{+2.56}_{-4.49}$	$-0.46^{+3.97}_{-2.29}$	$-2.49^{+0.35}_{-0.43}$	$-2.2^{+0.32}_{-0.85}$	$-4.4^{+1.7}_{-4.5}$
V	$-2.54^{+0.07}_{-0.09}$	$22.7^{+14.3}_{-13}$	$0.78^{+0.14}_{-0.40}$	$0.14^{+0.40}_{-0.13}$	$0.08^{+0.038}_{-0.032}$	$0.97^{+0.03}_{-0.06}$	$-5.61^{+2.72}_{-2.13}$	$2.61^{+2.18}_{-4.58}$	$-0.44^{+3.85}_{-2.31}$	$-2.43^{+0.28}_{-0.42}$	$-2.2^{+0.32}_{-0.87}$	$-4.6^{+1.7}_{-4.7}$
ROI = 95°square												
I	$-2.41^{+0.10}_{-0.13}$	$61^{+12.8}_{-56.1}$	$0.67^{+0.15}_{-0.49}$	$0.12^{+0.43}_{-0.11}$	$0.21^{+0.097}_{-0.064}$	$0.96^{+0.04}_{-0.05}$	$-4.78^{+2.54}_{-2.01}$	$2.71^{+2.08}_{-4.52}$	$0.05^{+3.85}_{-2.73}$	$-2.08^{+0.07}_{-0.29}$	$-2.3^{+0.57}_{-1.4}$	$-4.6^{+4}_{-6.2}$
II*	$-2.40^{+0.11}_{-0.12}$	$77.5^{+29.2}_{-65.2}$	$0.68^{+0.14}_{-0.42}$	$0.11^{+0.39}_{-0.10}$	$0.21^{+0.089}_{-0.064}$	$0.96^{+0.04}_{-0.05}$	$-4.89^{+2.60}_{-2.10}$	$2.62^{+2.16}_{-4.60}$	$-0.14^{+3.82}_{-2.57}$	$-2.11^{+0.10}_{-0.43}$	$-2.1^{+0.36}_{-1.1}$	$-5.1^{+2}_{-5.7}$
III	$-2.40^{+0.11}_{-0.12}$	$94.1^{+38}_{-64.9}$	$0.68^{+0.14}_{-0.38}$	$0.11^{+0.36}_{-0.10}$	$0.2^{+0.086}_{-0.063}$	$0.96^{+0.04}_{-0.05}$	$-4.94^{+2.59}_{-2.30}$	$2.52^{+2.24}_{-4.58}$	$-0.25^{+3.83}_{-2.47}$	$-2.17^{+0.15}_{-0.55}$	$-1.9^{+0.31}_{-0.87}$	$-4.5^{+1.7}_{-4.7}$
IV	$-2.40^{+0.11}_{-0.11}$	$95.8^{+38.4}_{-60.3}$	$0.68^{+0.14}_{-0.37}$	$0.11^{+0.35}_{-0.10}$	$0.2^{+0.084}_{-0.063}$	$0.96^{+0.04}_{-0.05}$	$-4.85^{+2.52}_{-2.32}$	$2.44^{+2.35}_{-4.50}$	$-0.32^{+3.91}_{-2.41}$	$-2.18^{+0.16}_{-0.54}$	$-1.9^{+0.31}_{-0.8}$	$-4.4^{+1.7}_{-4.3}$
V	$-2.37^{+0.10}_{-0.12}$	$51.1^{+24.4}_{-40.7}$	$0.69^{+0.13}_{-0.41}$	$0.11^{+0.38}_{-0.10}$	$0.19^{+0.085}_{-0.059}$	$0.96^{+0.04}_{-0.05}$	$-4.66^{+2.42}_{-2.18}$	$2.60^{+2.19}_{-4.62}$	$-0.23^{+3.81}_{-2.50}$	$-2.11^{+0.10}_{-0.30}$	$-2^{+0.33}_{-1.1}$	$-4.8^{+1.8}_{-5.7}$

*: Benchmark ISM model

#: The quantities $\dot{n}_{\rm inj}$, $\mathcal{N}_{\rm CMB}$ and $\mathcal{N}_{\rm UPS}$ are normalized to the effective area $4\pi D^2$, and in units of cm^{-2} s^{-1}, following Table A1 of the main paper.

TABLE S2: Posteriors on model parameters in the various choices of ISM composition (I-V) as described earlier. The posteriors reported for each case correspond to the scaling model with the highest Bayes factor (see Table S1). The median value of the posterior on each parameter is reported along with its difference from the 5th and 95th percentiles.

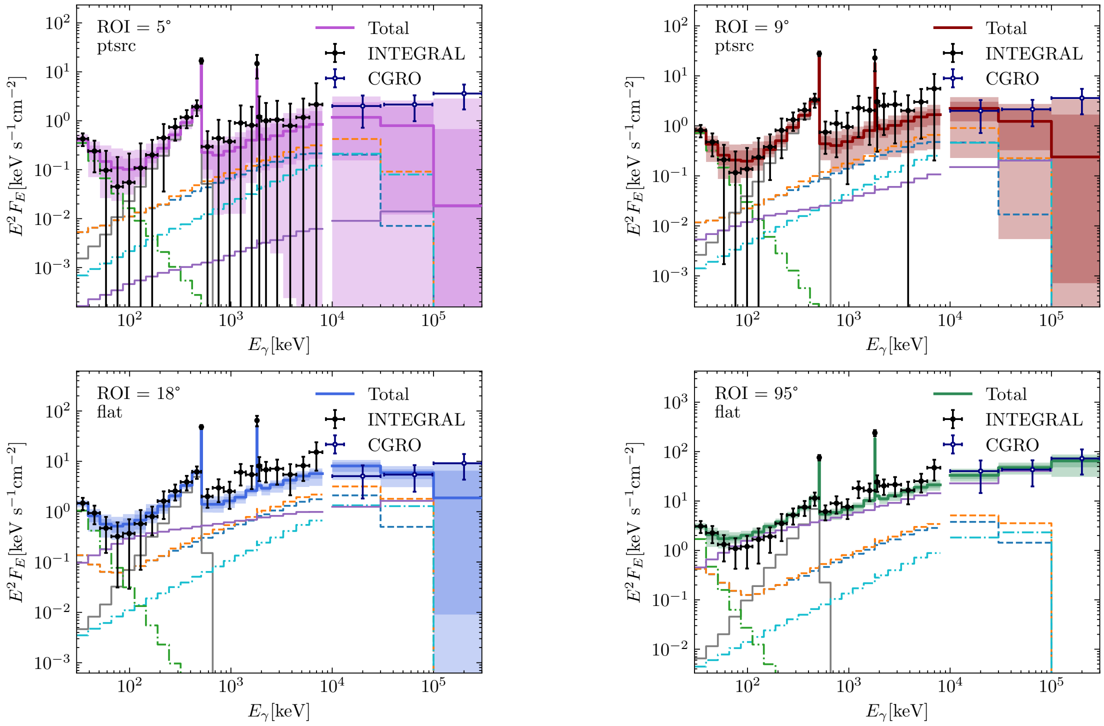

FIG. S2: Median spectral fits for each region of interest (using the scaling model with highest Bayes factor), similar to Figure 2 of main paper, for an ionized medium with $f_{\rm IC} = 10^{-5}$ (ISM model I). The individual components of the γ-ray emission are labeled the same way as in Fig. 2 of the main paper.

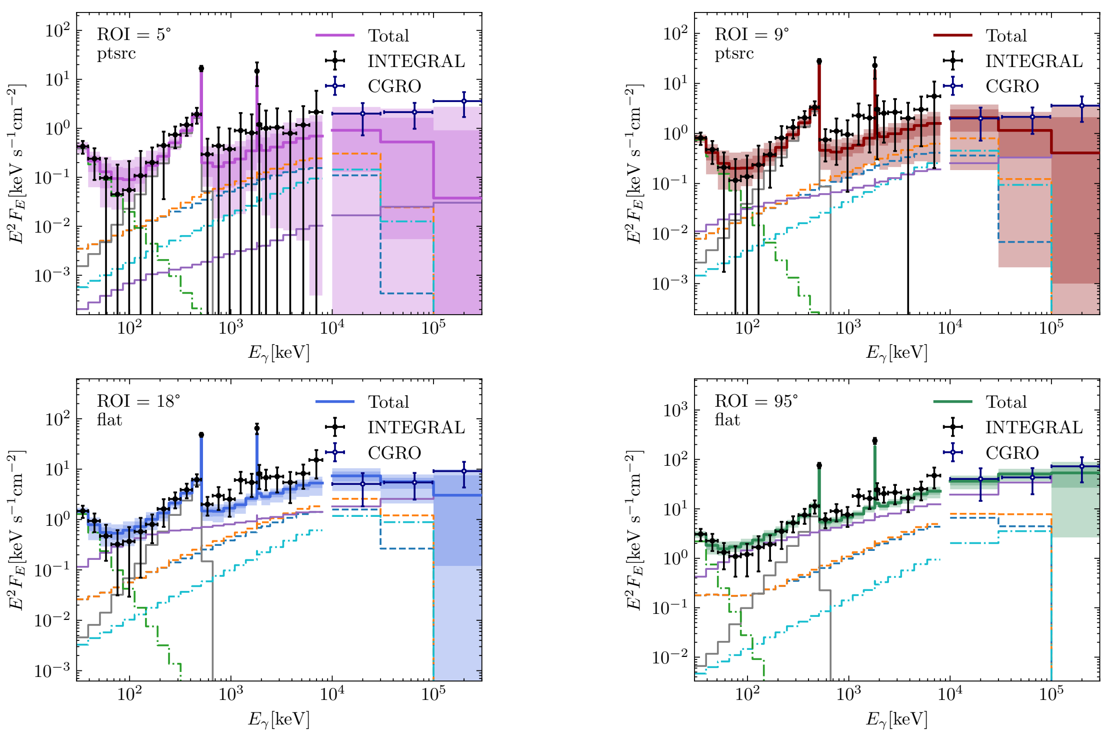

FIG. S3: Same as S2, for the fiducial ISM model (II).

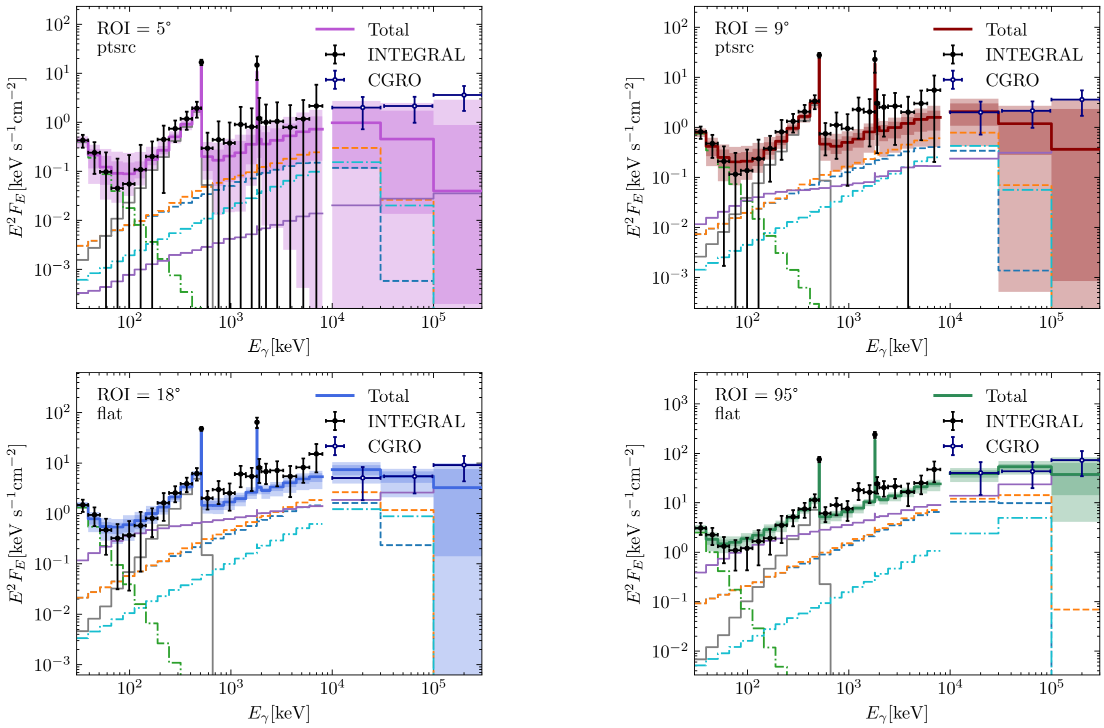

FIG. S4: Same as S2, for an ionized medium with $f_{\rm IC} = 10^{-7}$ (III)

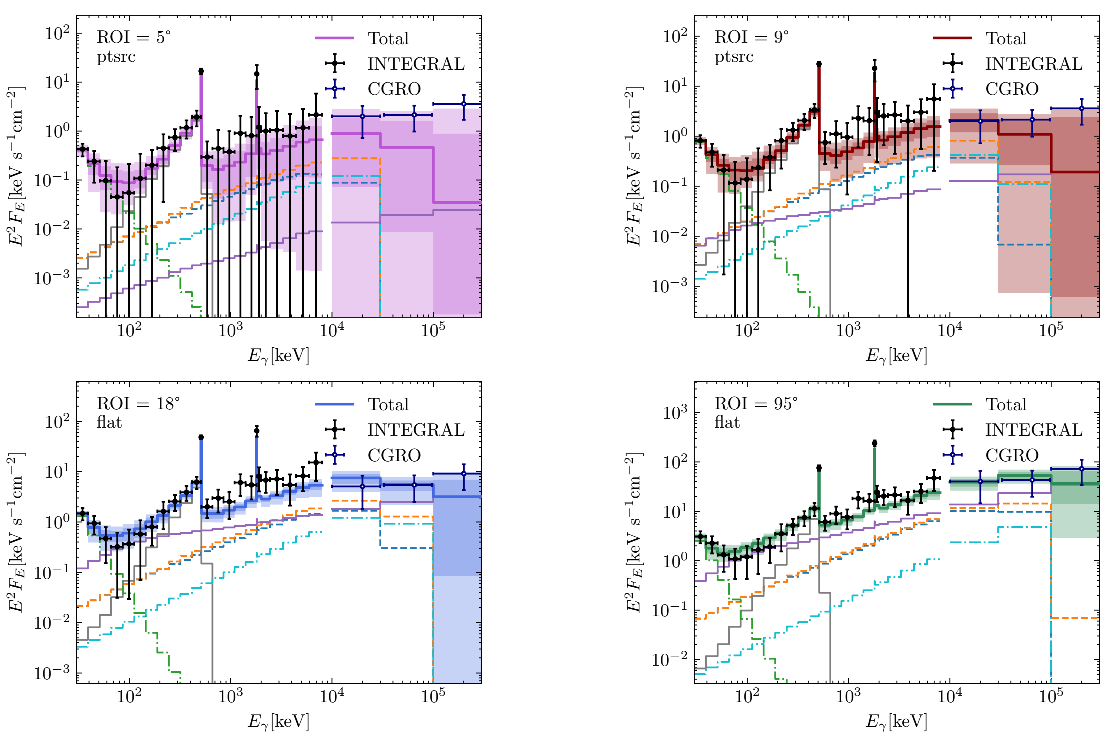

FIG. S5: Same as S2, for an ionized medium with $f_{\rm IC} = 10^{-8}$ (IV)

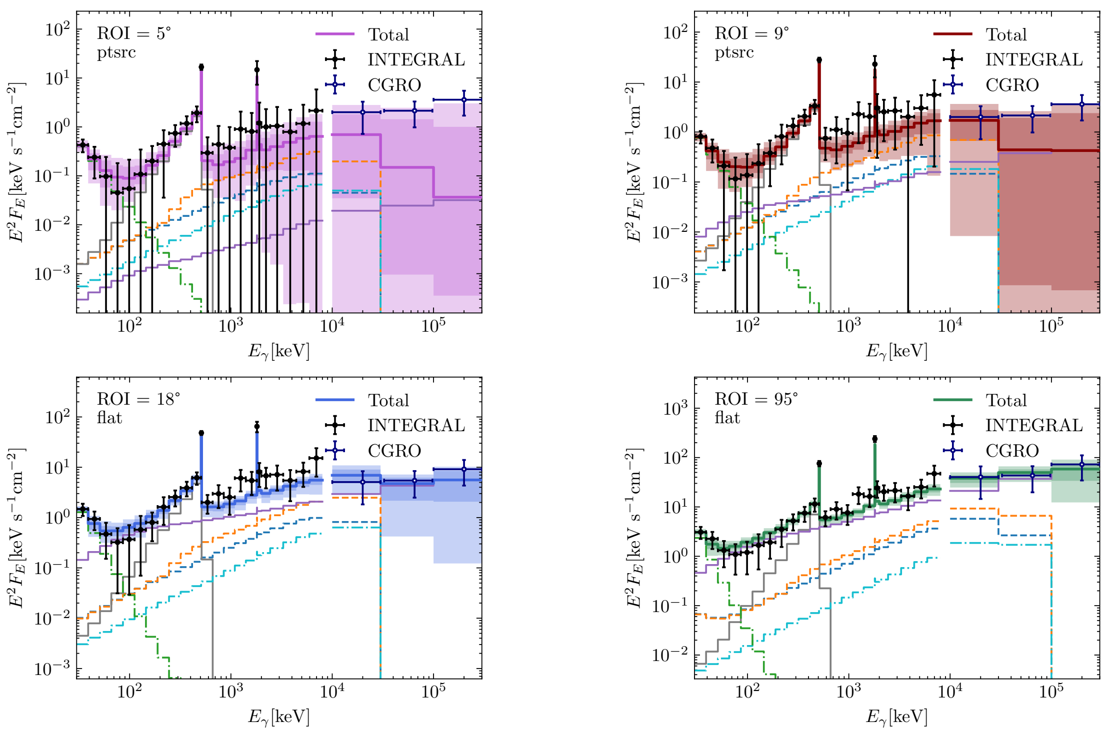

FIG. S6: Same as S2, for an atomic medium with $f_{\rm IC} = 10^{-6}$ (V)

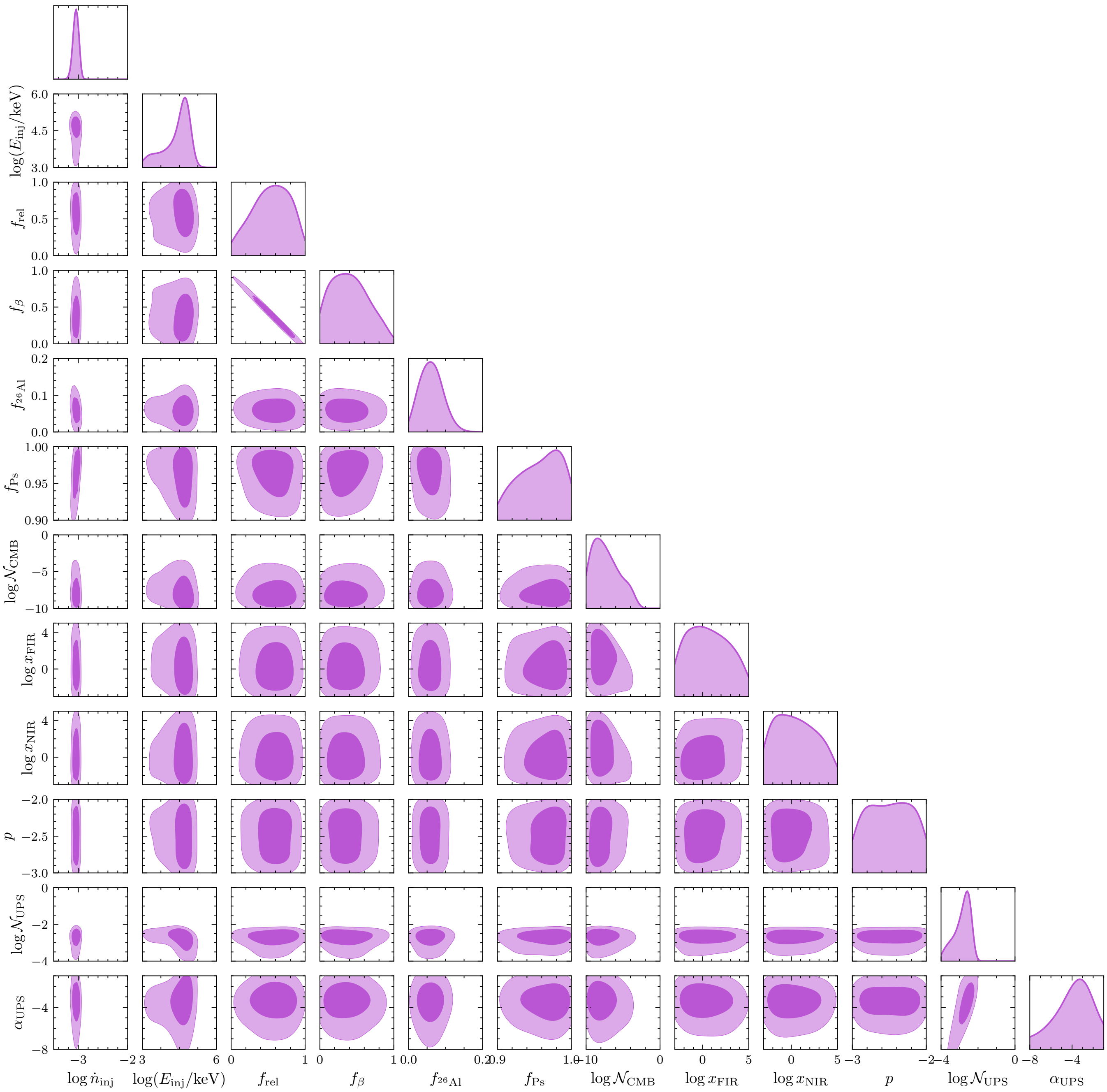

FIG. S7: Full posteriors for (I) ionized medium, $f_{\rm IC} = 10^{-5}$, for the 5° ROI. We use the convention of Table A1 for the units and normalization of each of these parameters. $E_{\rm inj}$ is in units of keV.

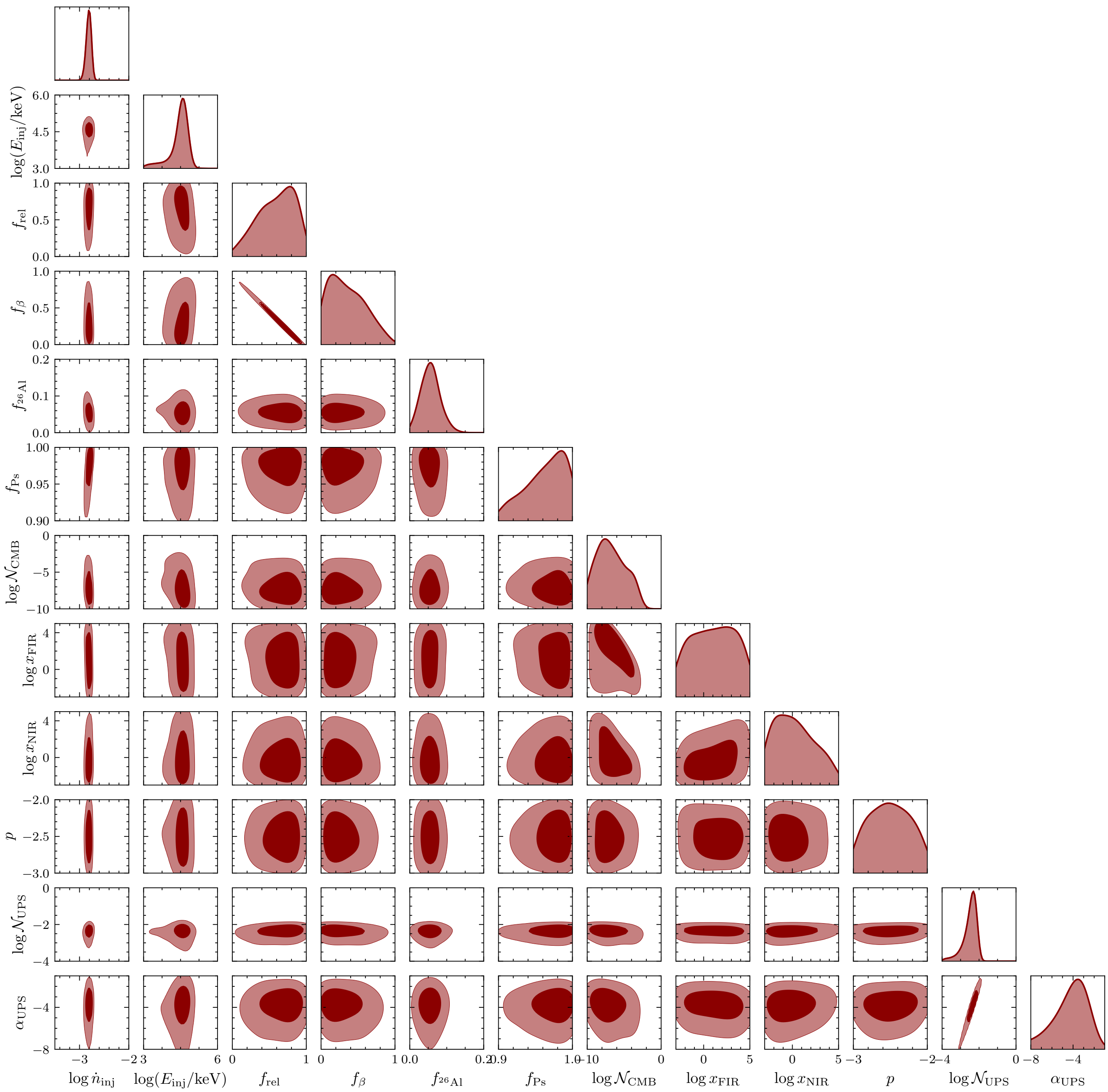

FIG. S8: Full posteriors for (I) ionized medium, $f_{\rm IC} = 10^{-5}$, for the 9° ROI.

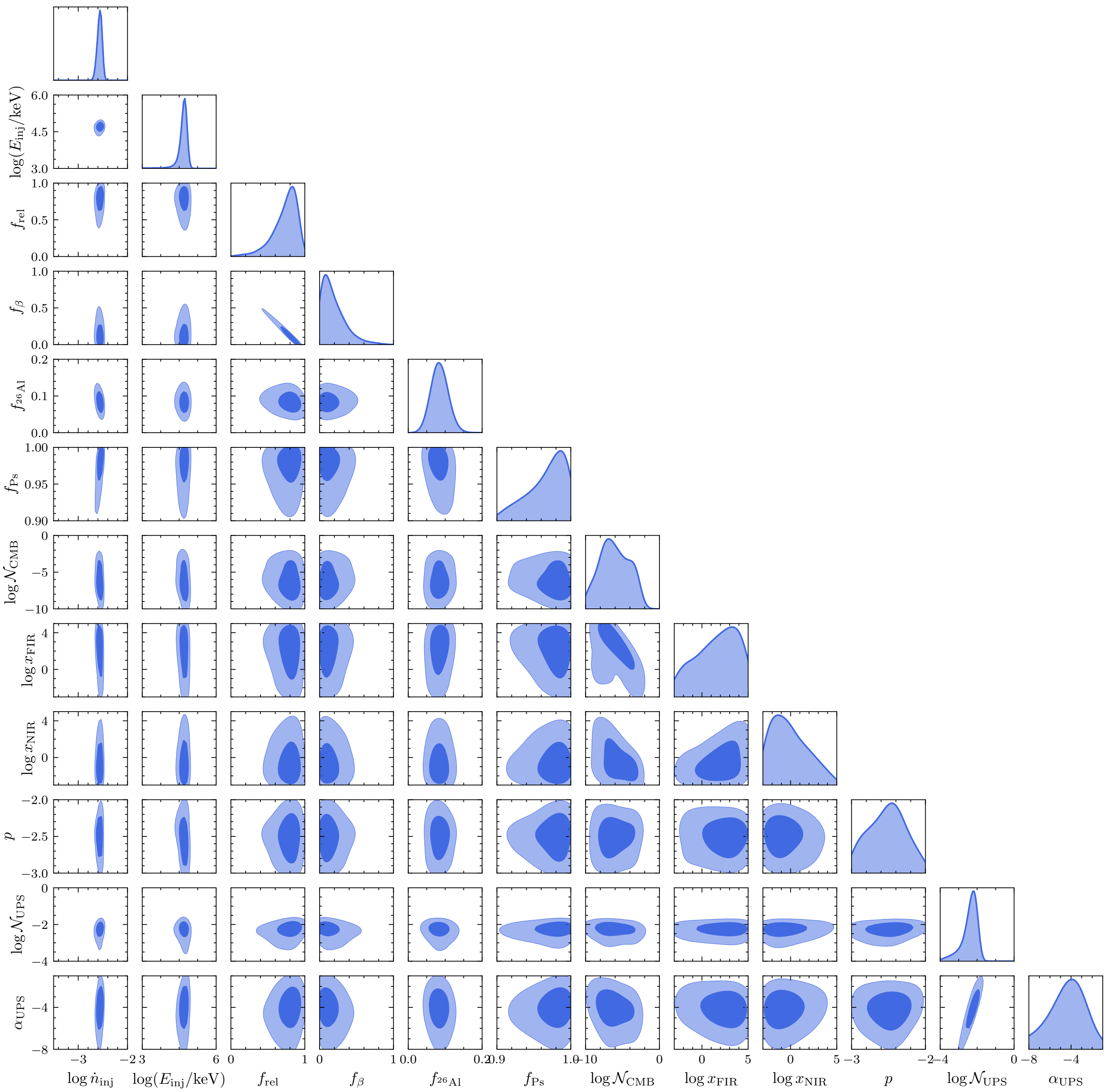

FIG. S9: Full posteriors for (I) ionized medium, $f_{\rm IC} = 10^{-5}$, for the 18° ROI.

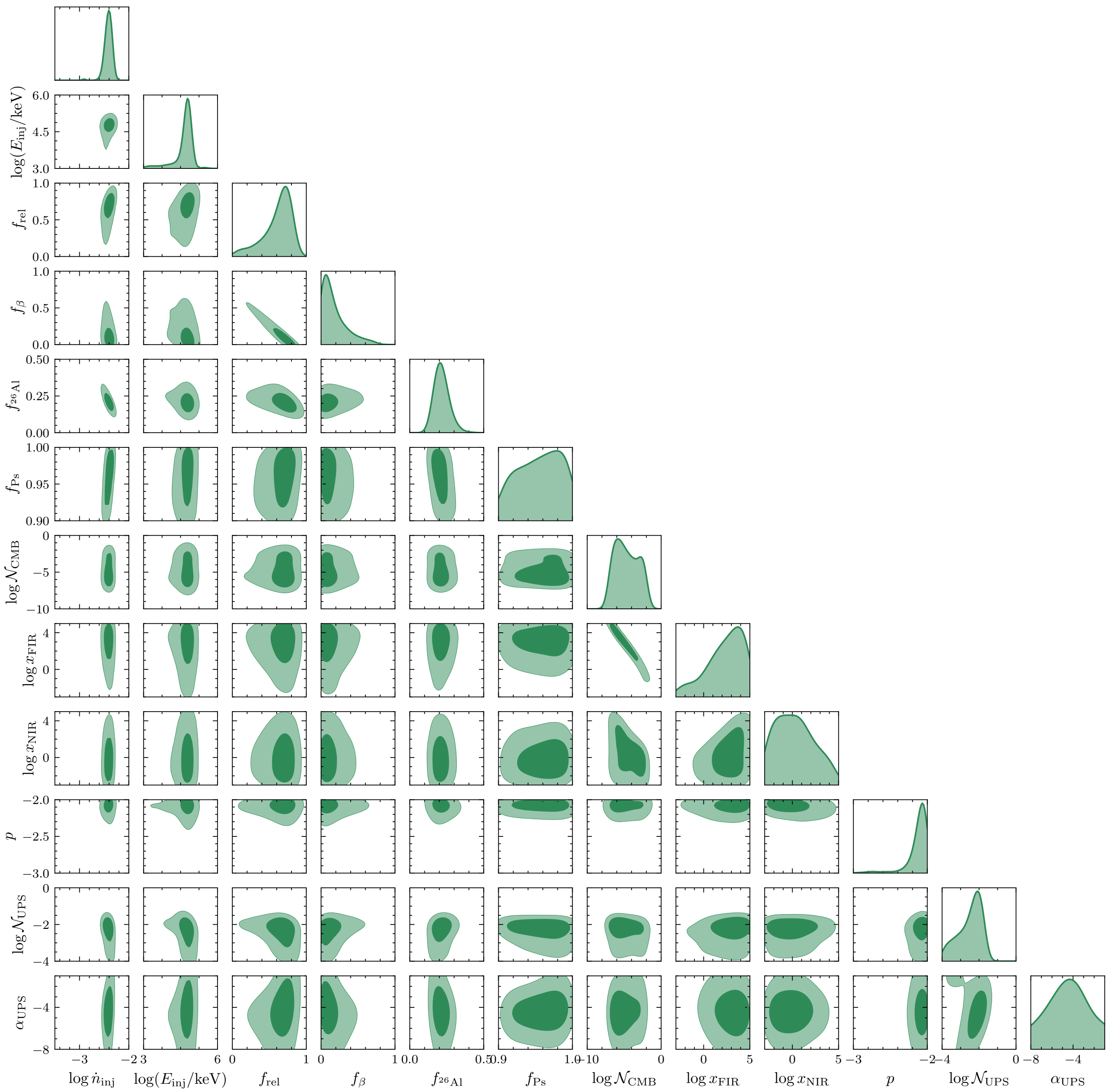

FIG. S10: Full posteriors for (I) ionized medium, $f_{\rm IC} = 10^{-5}$, for the 95° ROI.

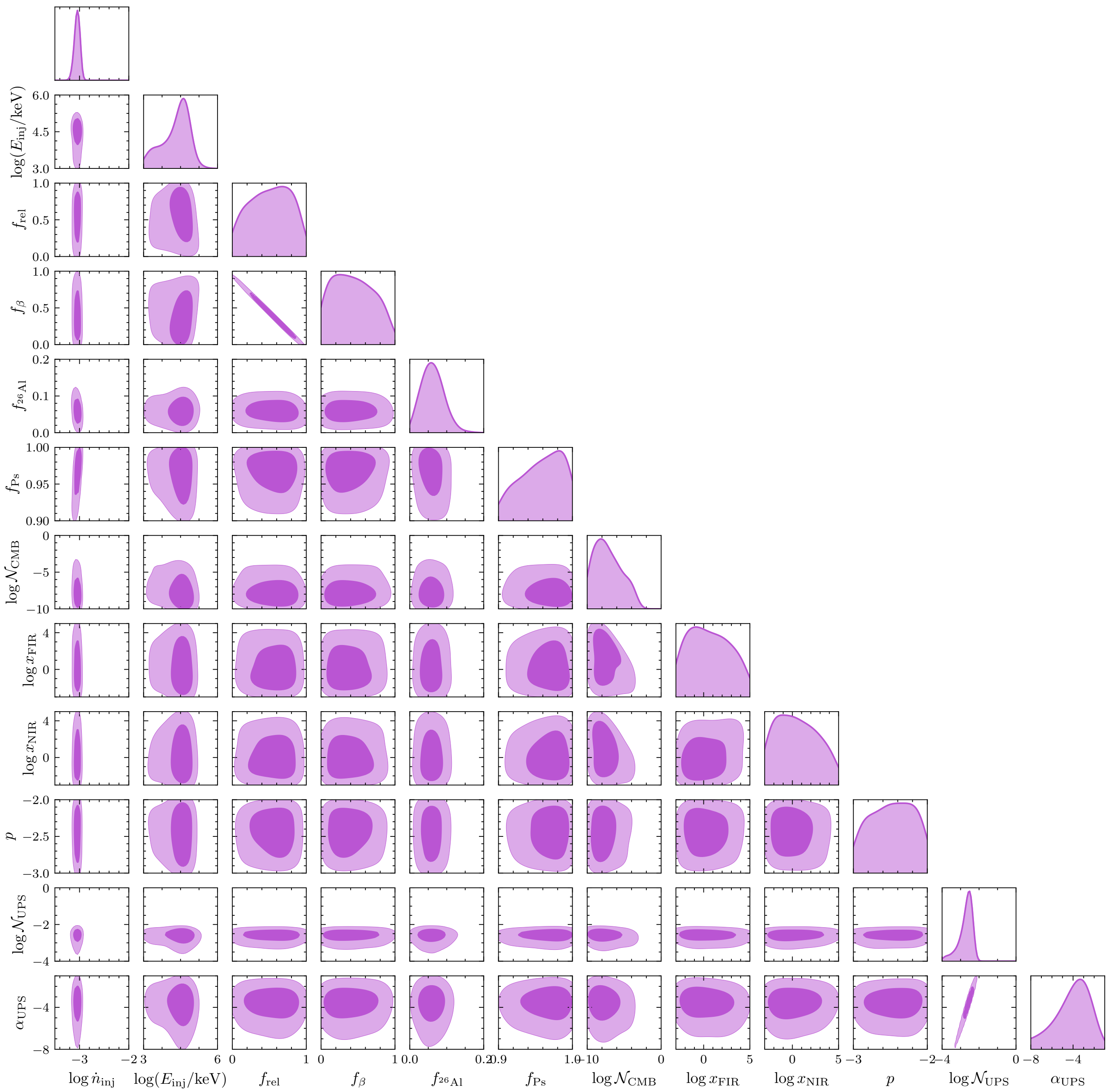

FIG. S11: Full posteriors for (II; benchmark ISM model) ionized medium, $f_{\rm IC} = 10^{-6}$, for the 5° ROI.

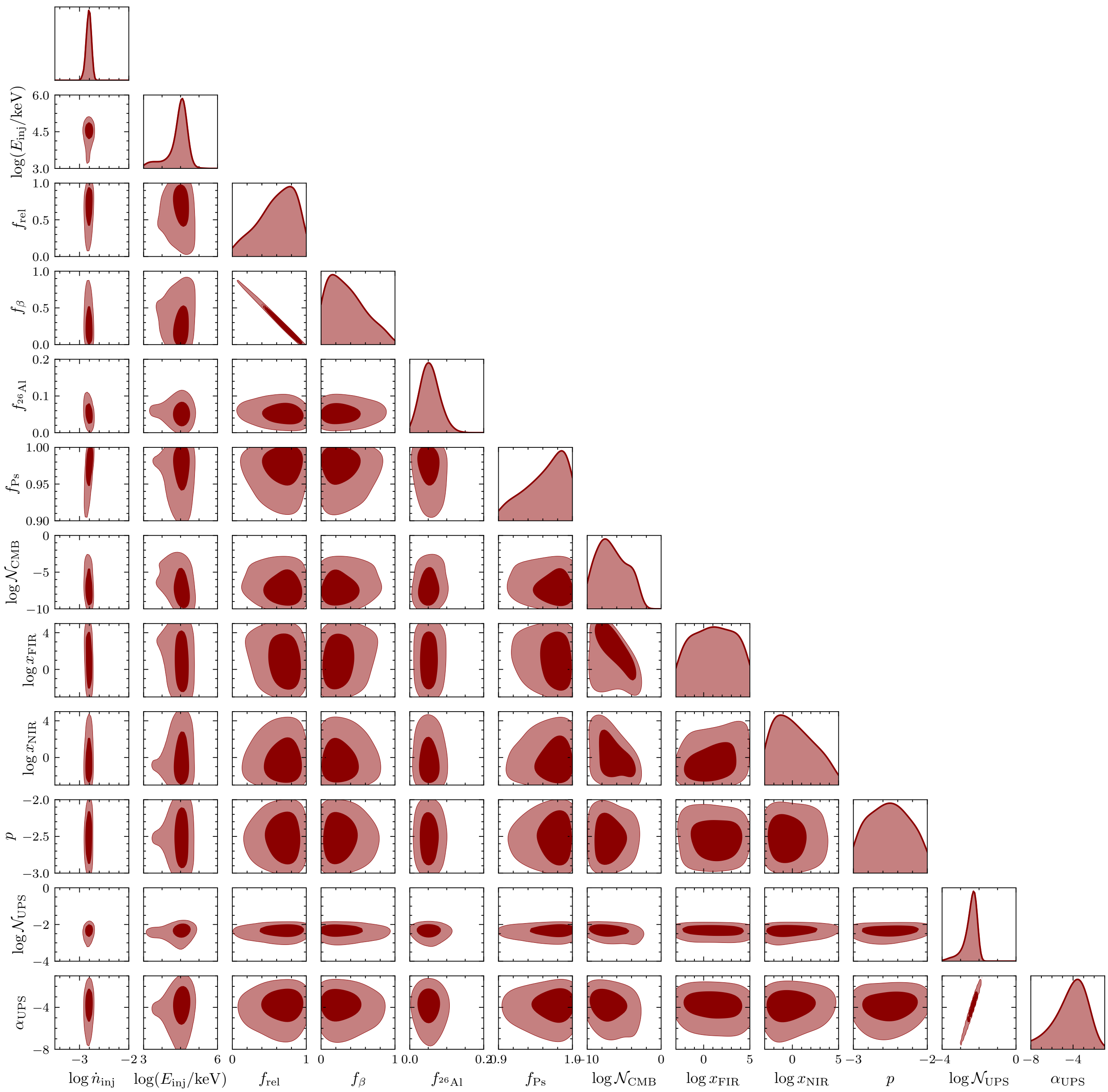

FIG. S12: Full posteriors for (II; benchmark ISM model) ionized medium, $f_{\rm IC} = 10^{-6}$, for the 9° ROI.

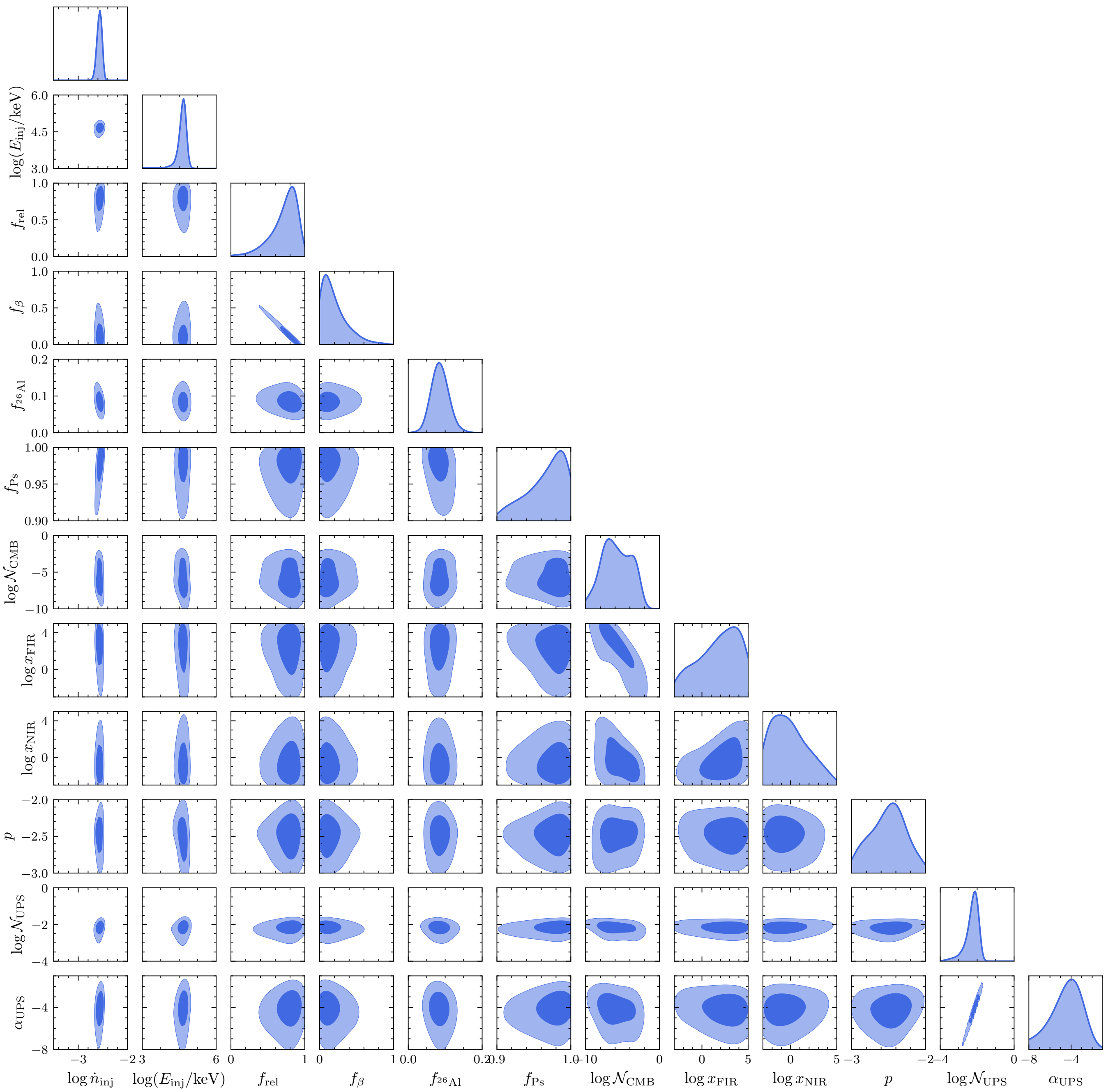

FIG. S13: Full posteriors for (II; benchmark ISM model) ionized medium, $f_{IC} = 10^{-6}$, for the 18° ROI.

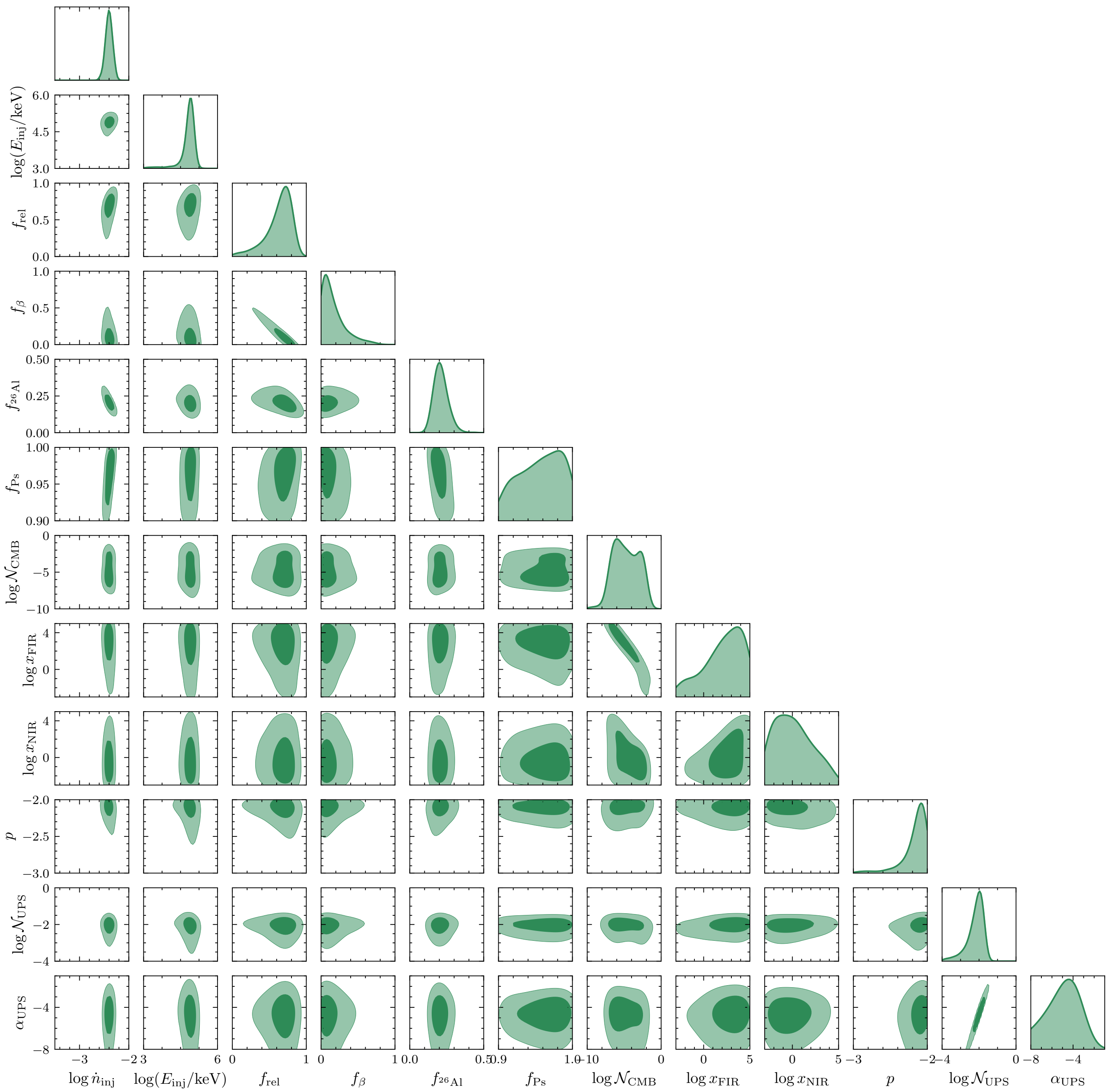

FIG. S14: Full posteriors for (II; benchmark ISM model) ionized medium, $f_{\rm IC} = 10^{-6}$, for the 95° ROI.

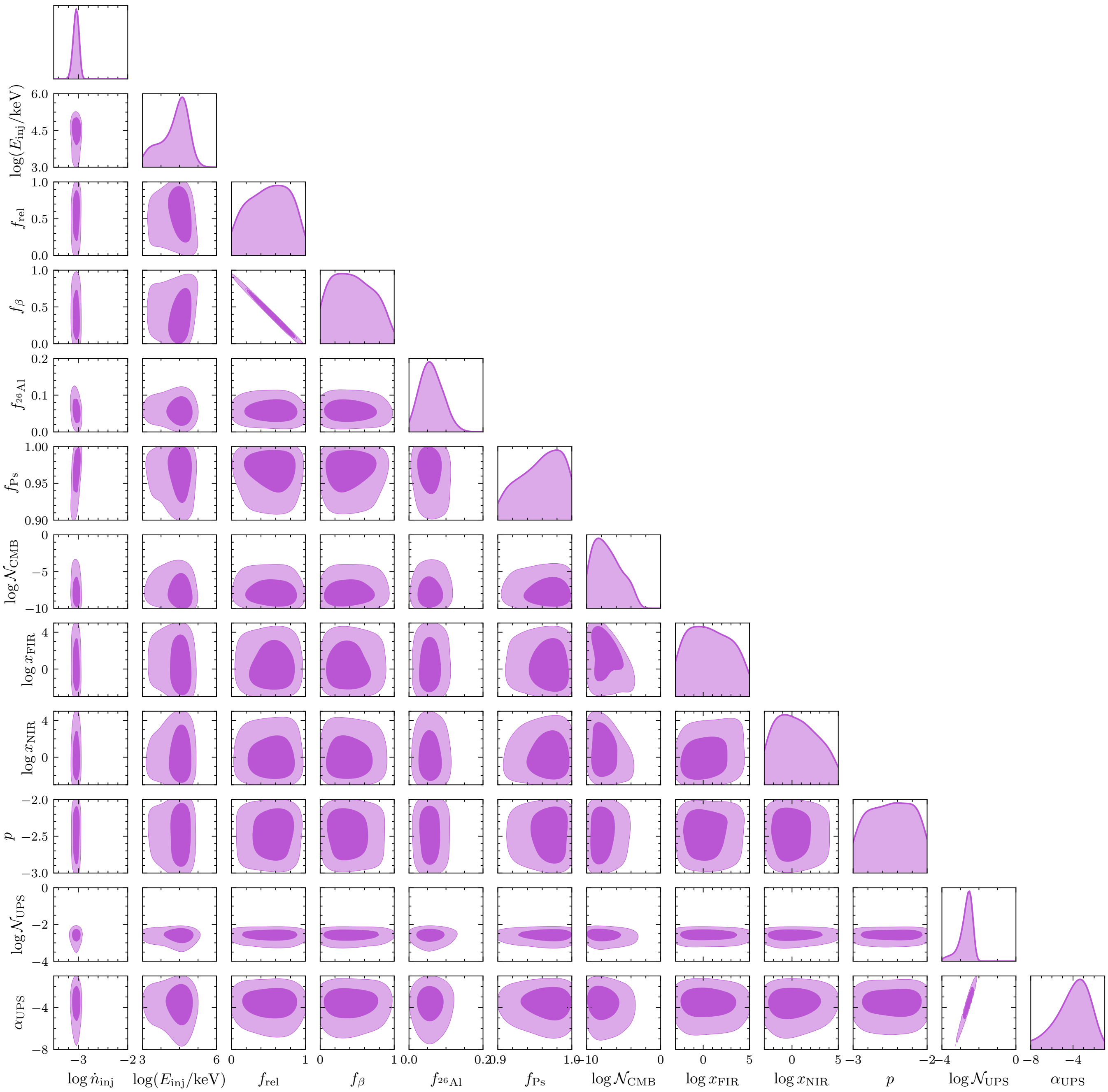

FIG. S15: Full posteriors for (III) ionized medium, $f_{\rm IC} = 10^{-7}$, for the 5° ROI.

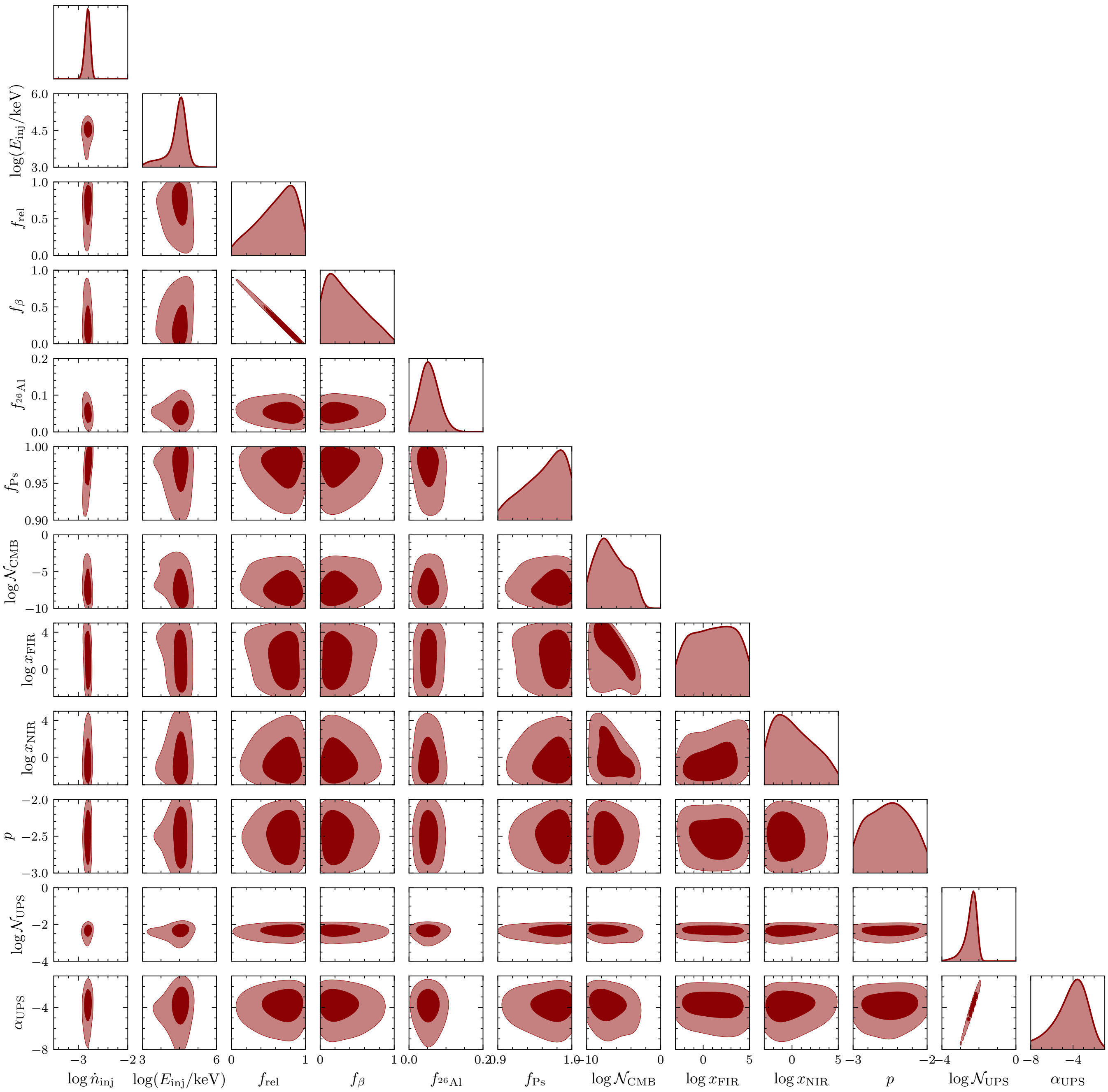

FIG. S16: Full posteriors for (III) ionized medium, $f_{\rm IC} = 10^{-7}$, for the 9° ROI.

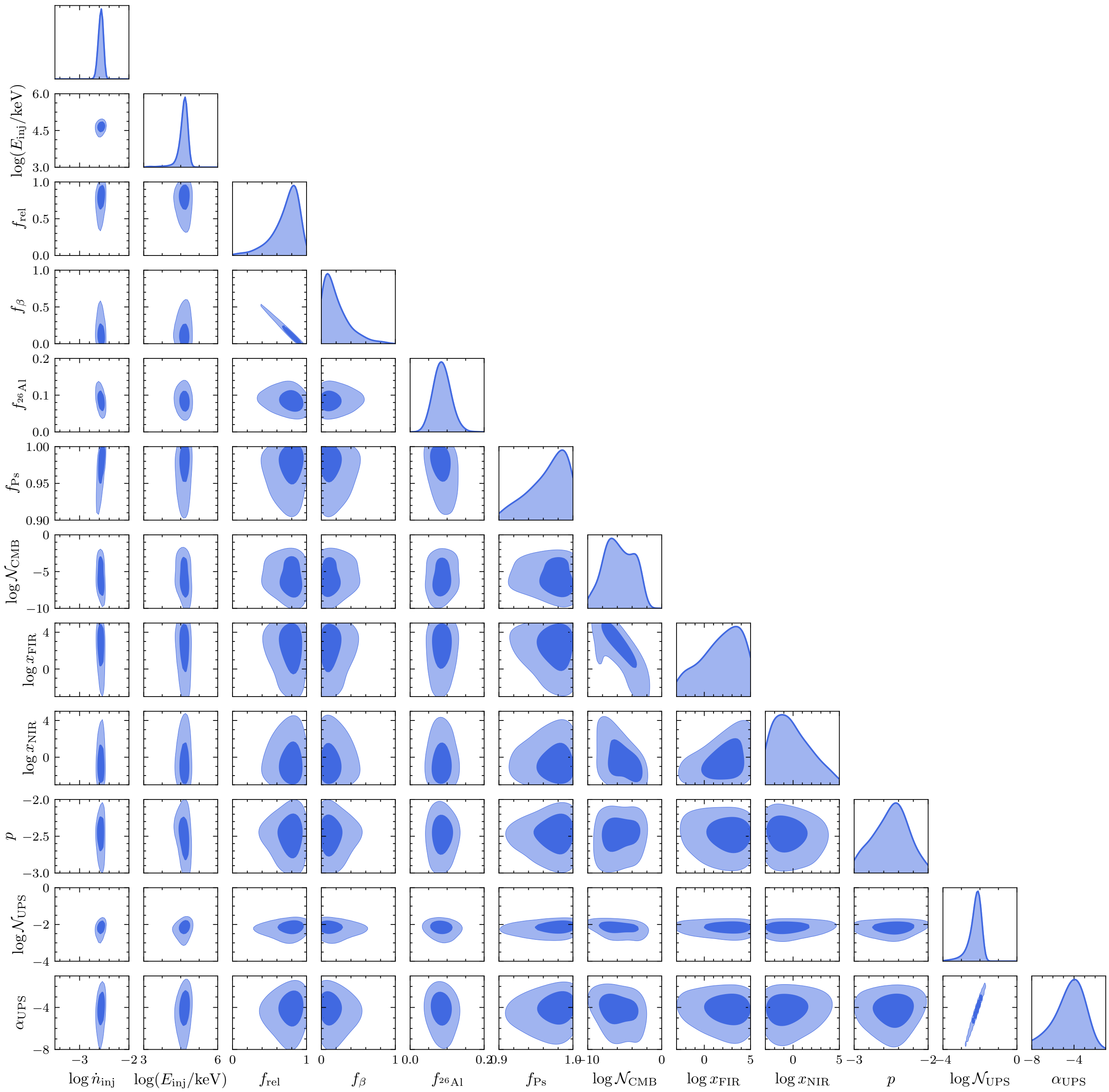

FIG. S17: Full posteriors for (III) ionized medium, $f_{\rm IC} = 10^{-7}$, for the 18° ROI.

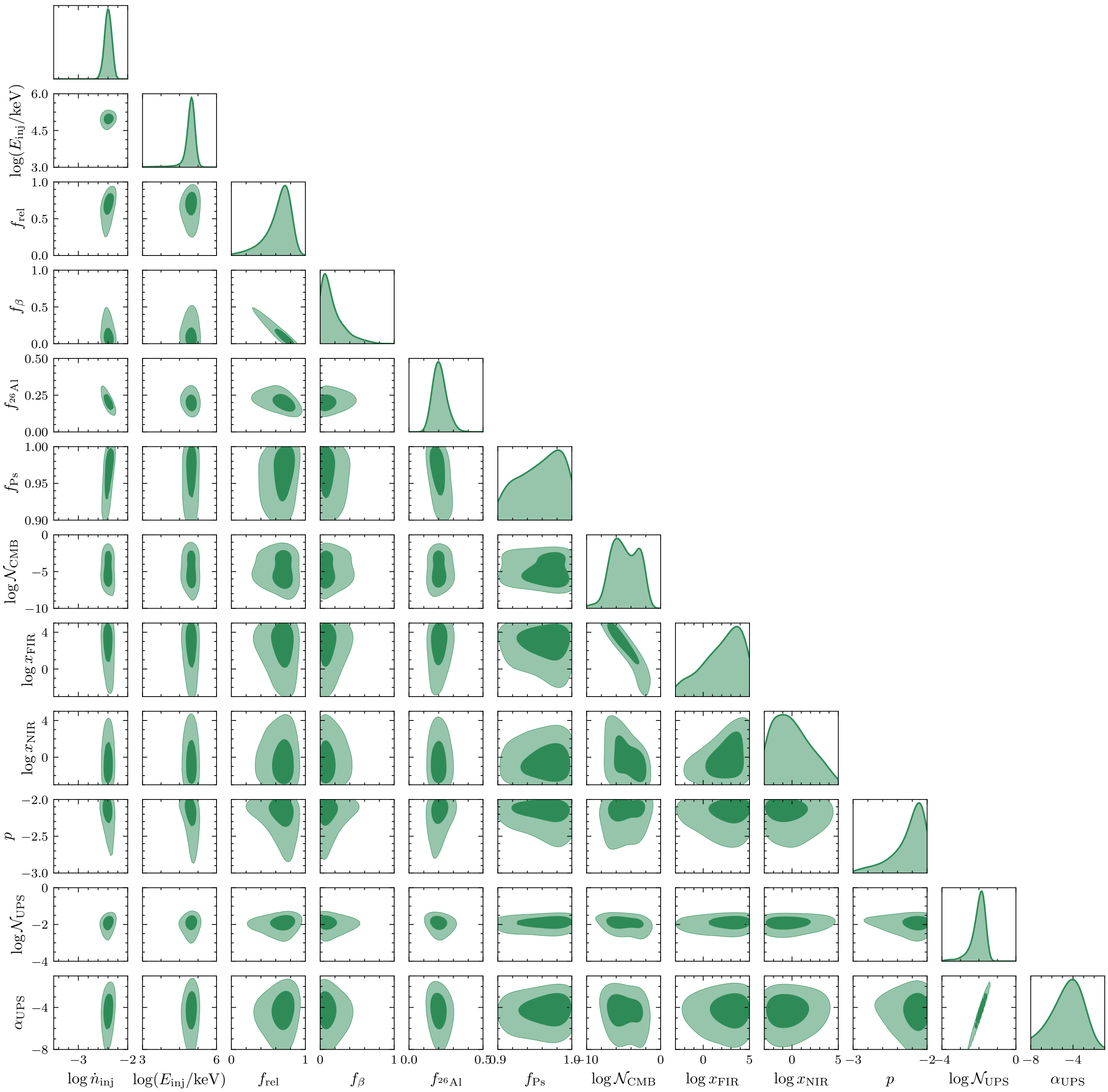

FIG. S18: Full posteriors for (III) ionized medium, $f_{\rm IC} = 10^{-7}$, for the 95° ROI.

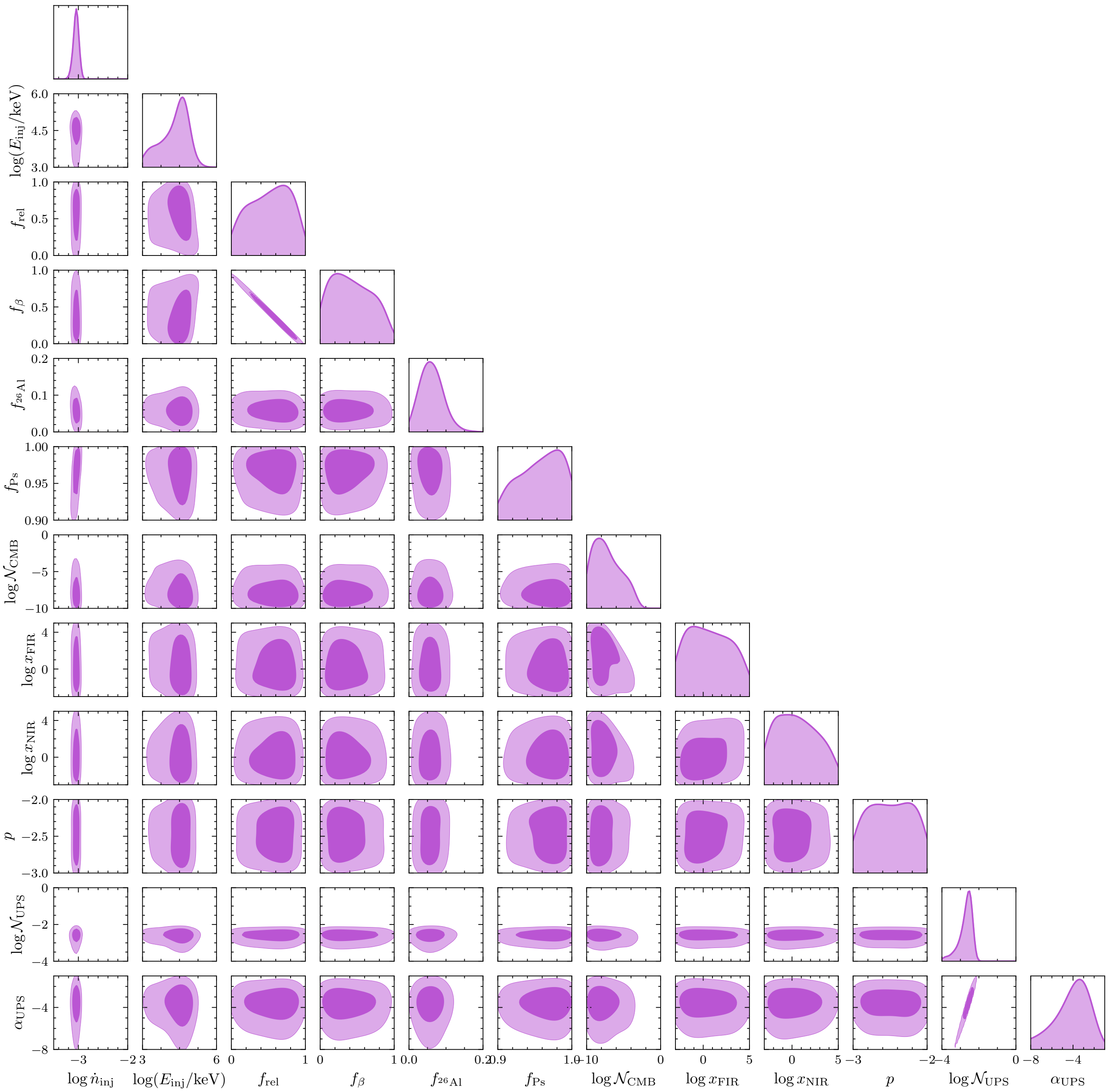

FIG. S19: Full posteriors for (IV) ionized medium, $f_{\rm IC} = 10^{-8}$, for the 5° ROI.

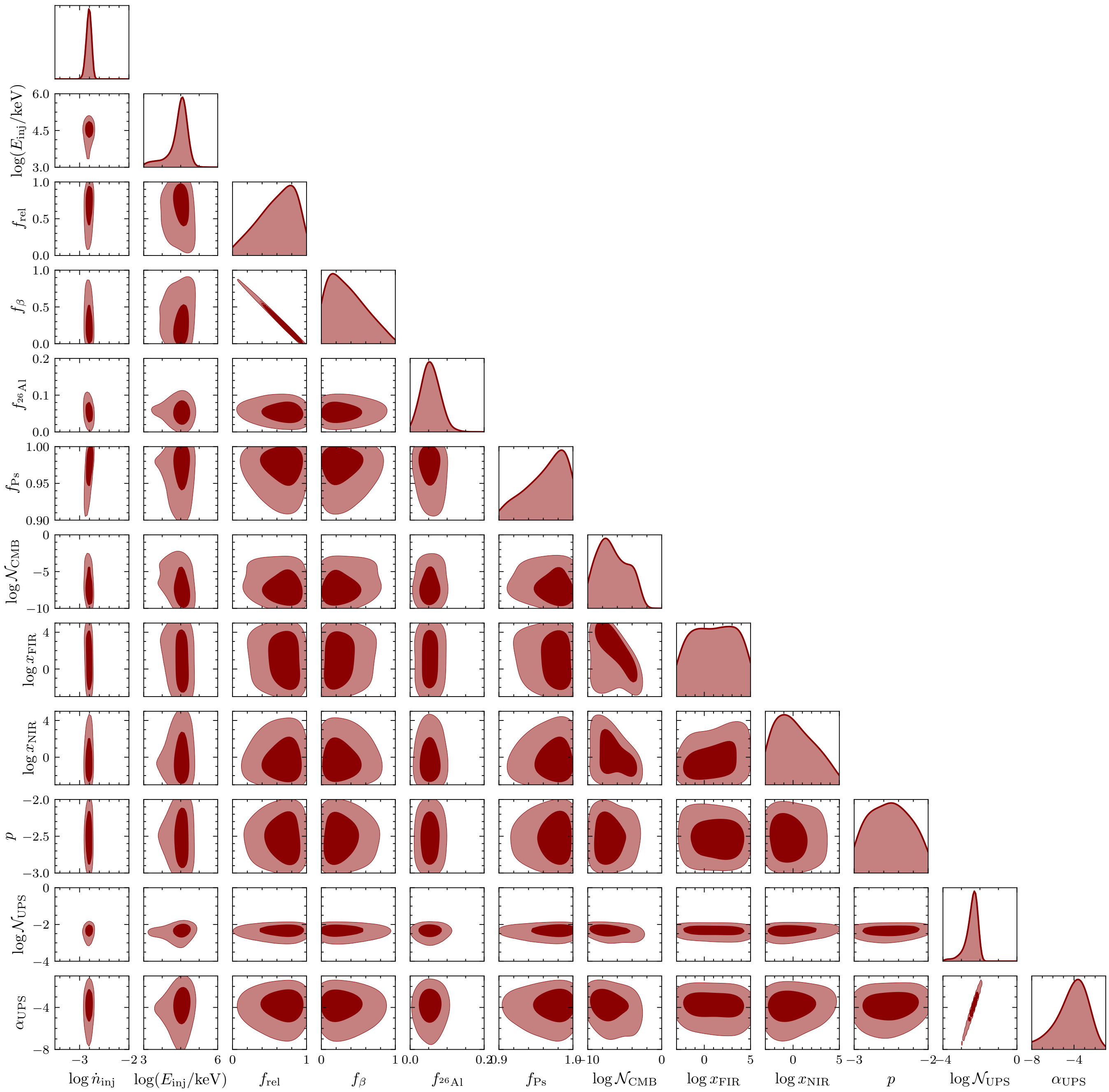

FIG. S20: Full posteriors for (IV) ionized medium, $f_{\rm IC} = 10^{-8}$, for the 9° ROI.

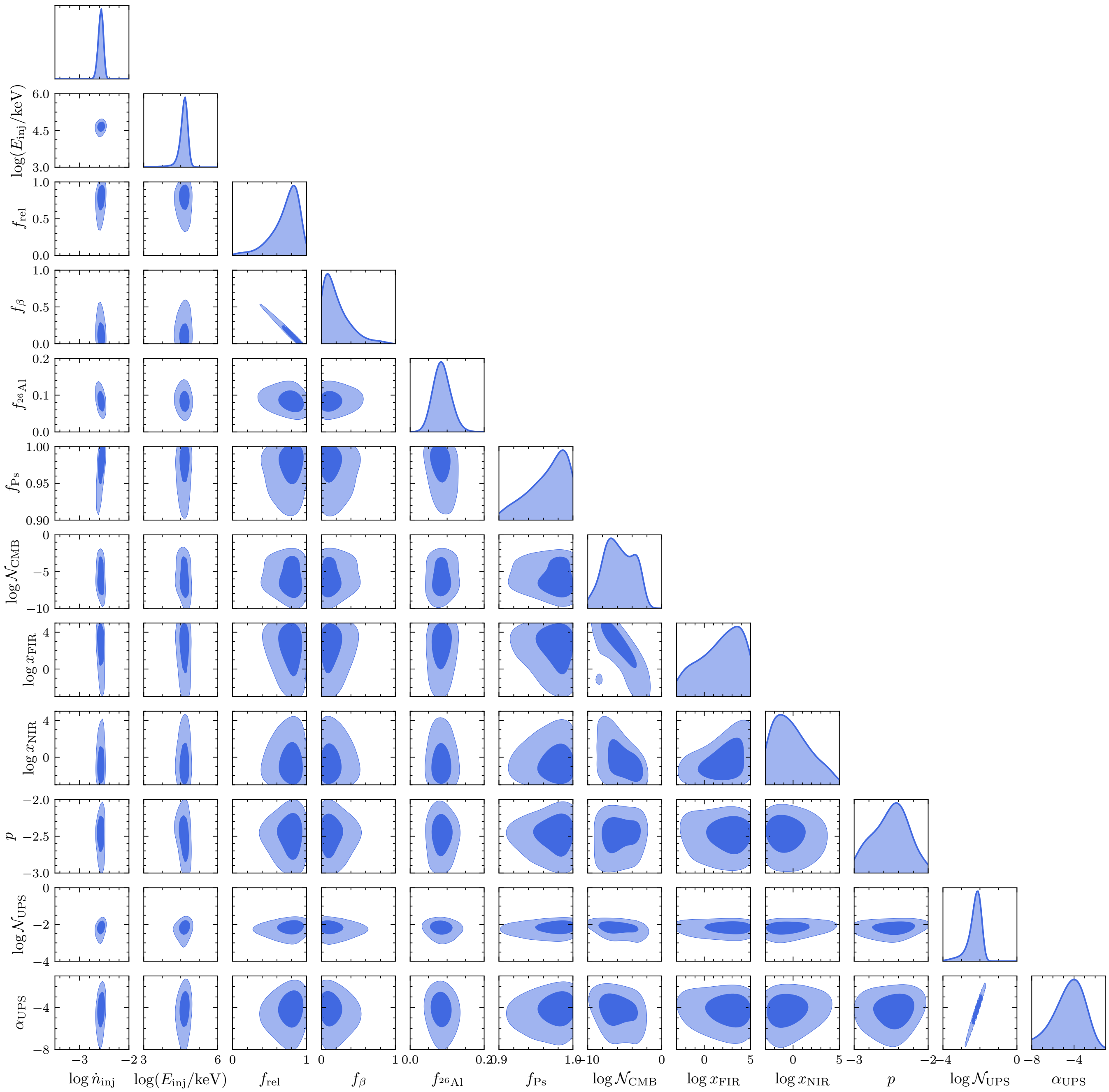

FIG. S21: Full posteriors for (IV) ionized medium, $f_{\rm IC} = 10^{-8}$, for the 18° ROI.

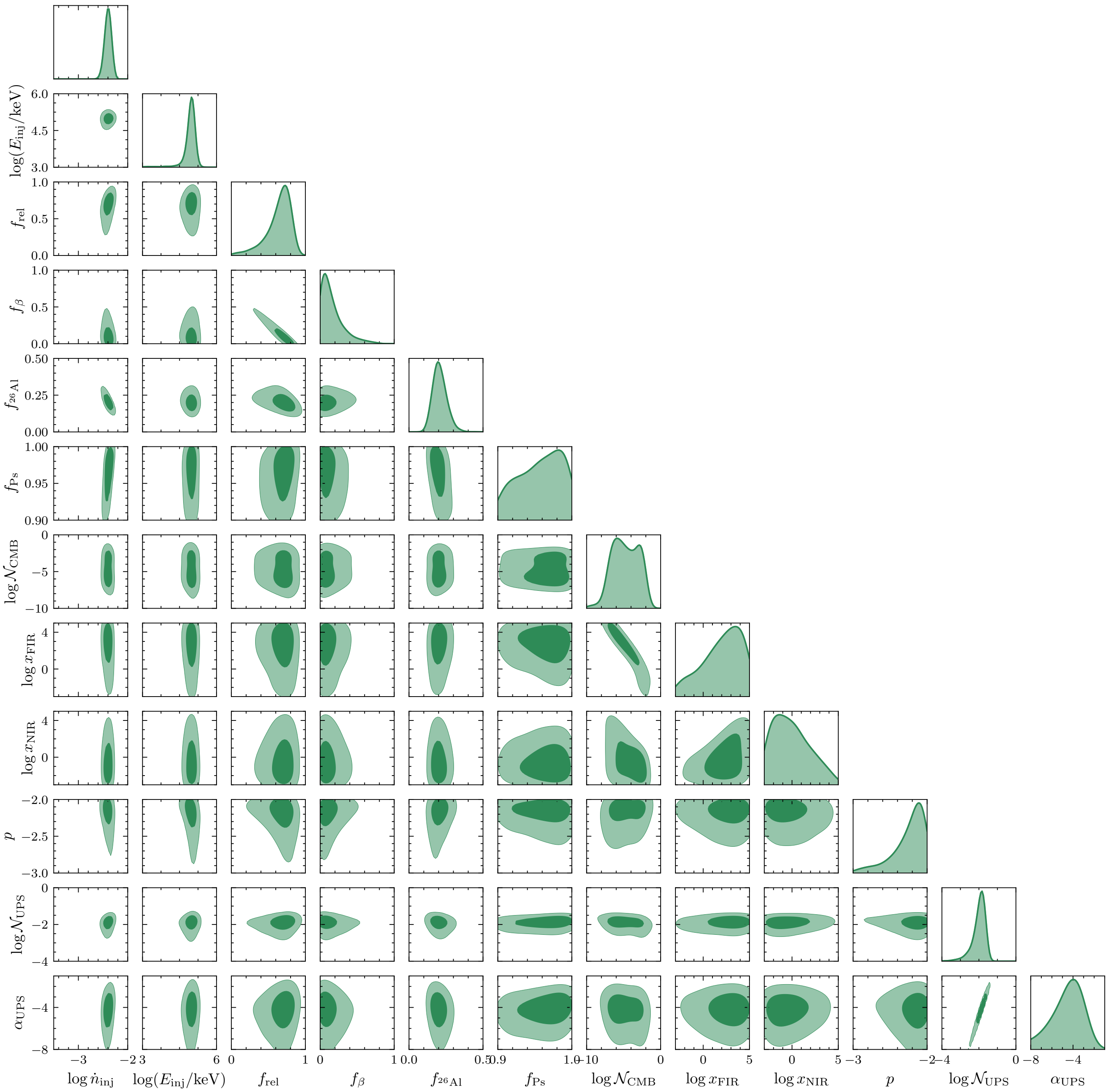

FIG. S22: Full posteriors for (IV) ionized medium, $f_{\rm IC} = 10^{-8}$, for the 95° ROI.

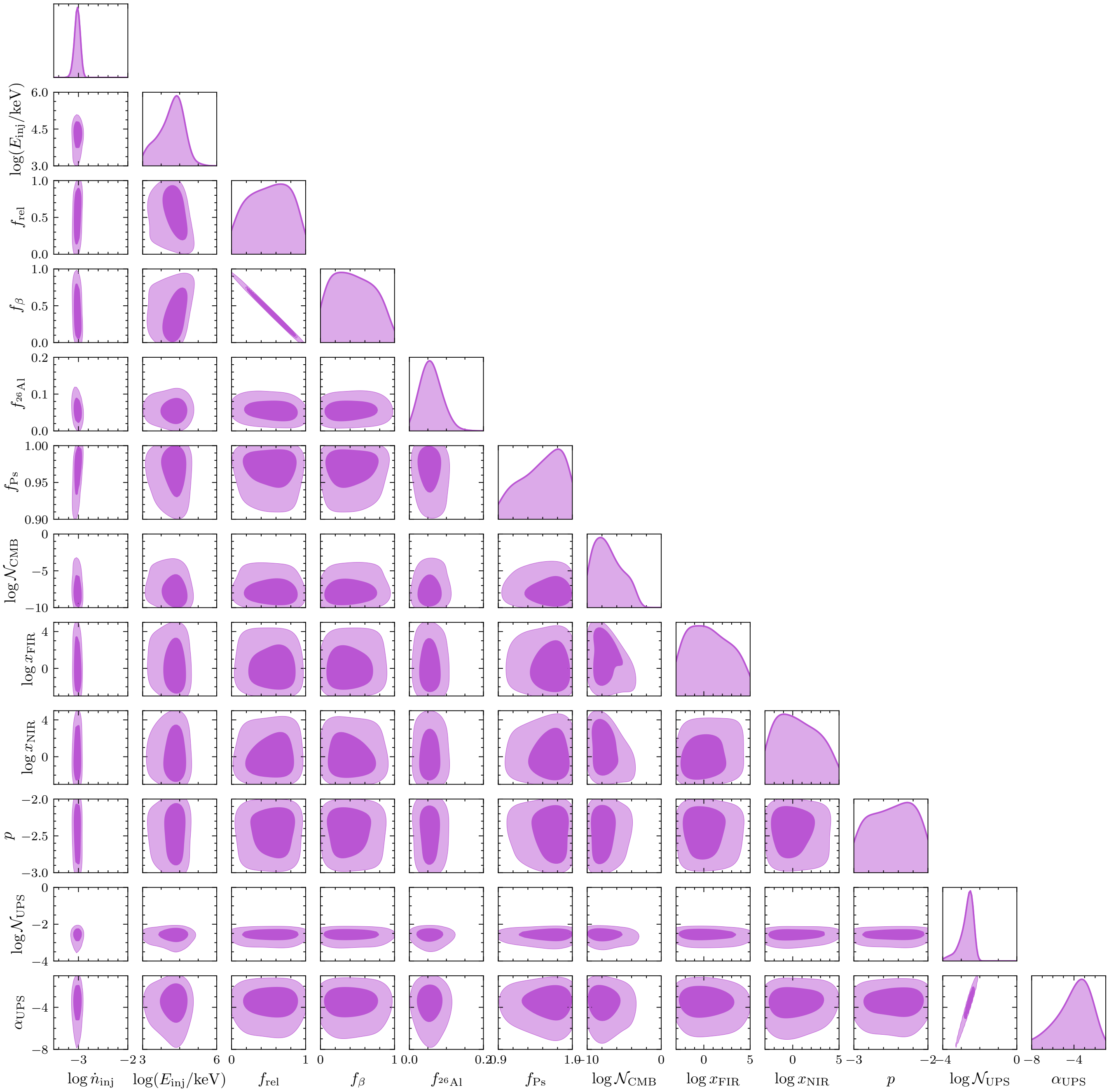

FIG. S23: Full posteriors for (V) atomic medium, $f_{\rm IC} = 10^{-6}$, for the 5° ROI.

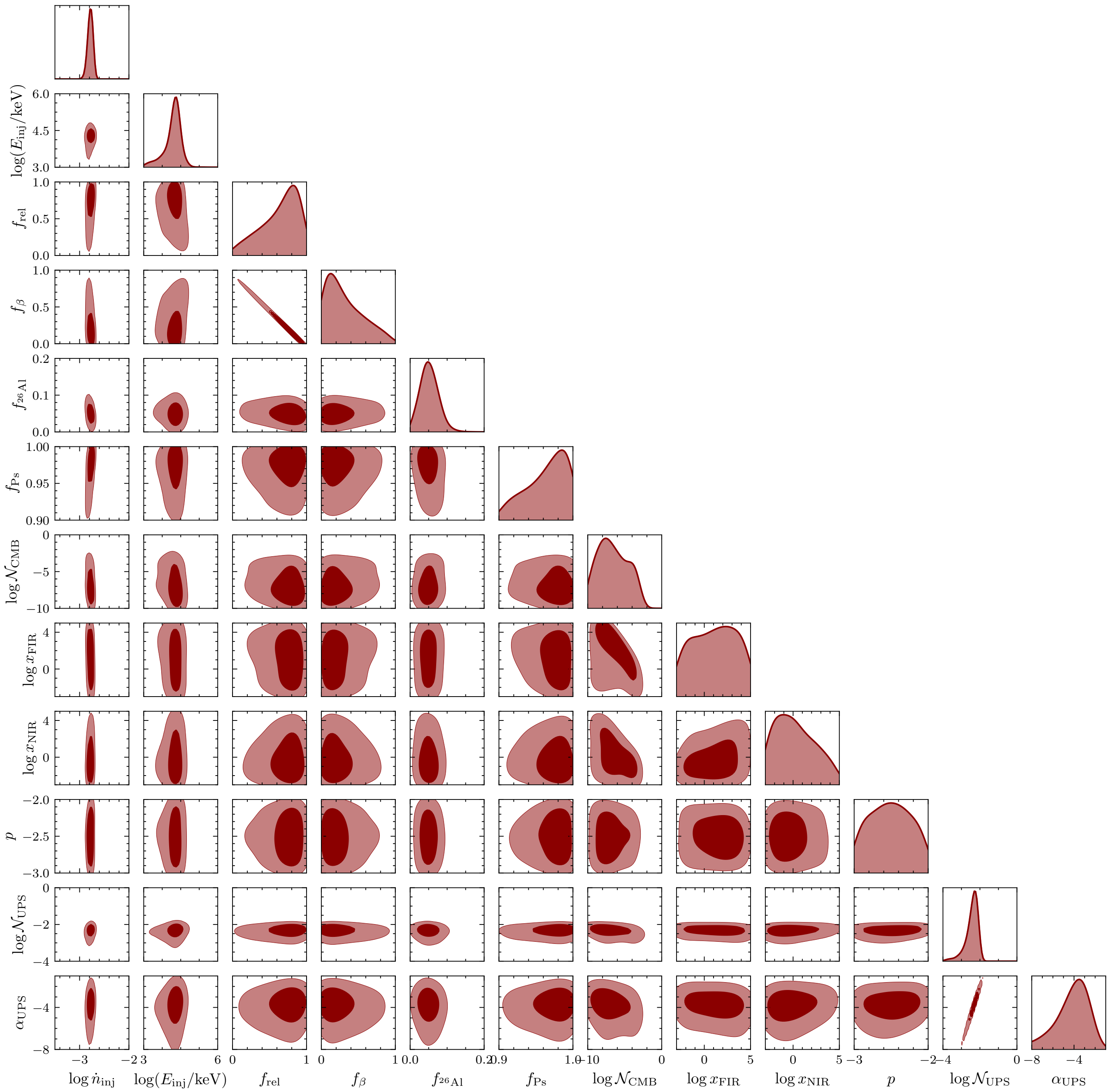

FIG. S24: Full posteriors for (V) atomic medium, $f_{\rm IC} = 10^{-6}$, for the 9° ROI.

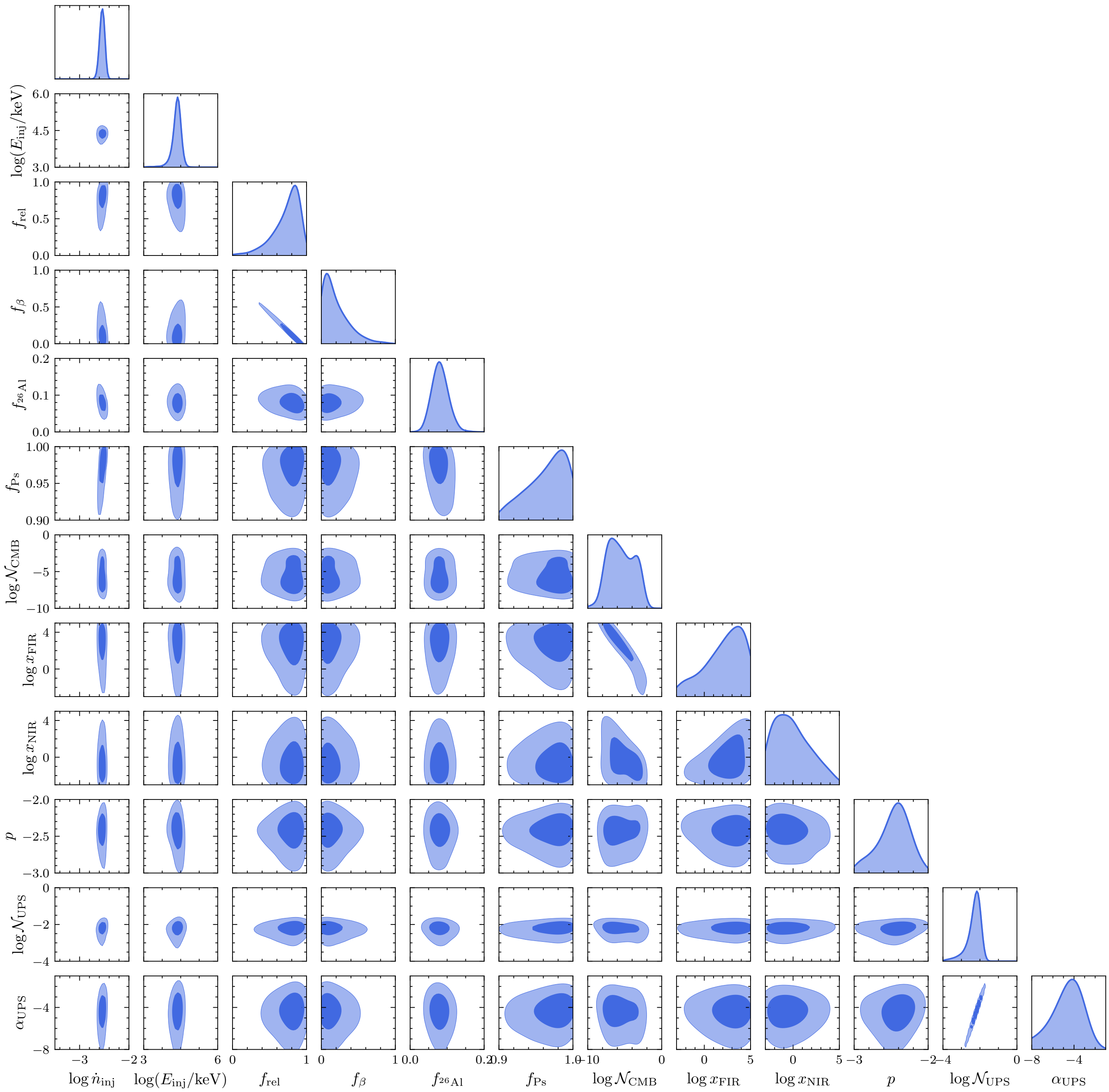

FIG. S25: Full posteriors for (V) atomic medium, $f_{\rm IC} = 10^{-6}$, for the 18° ROI.

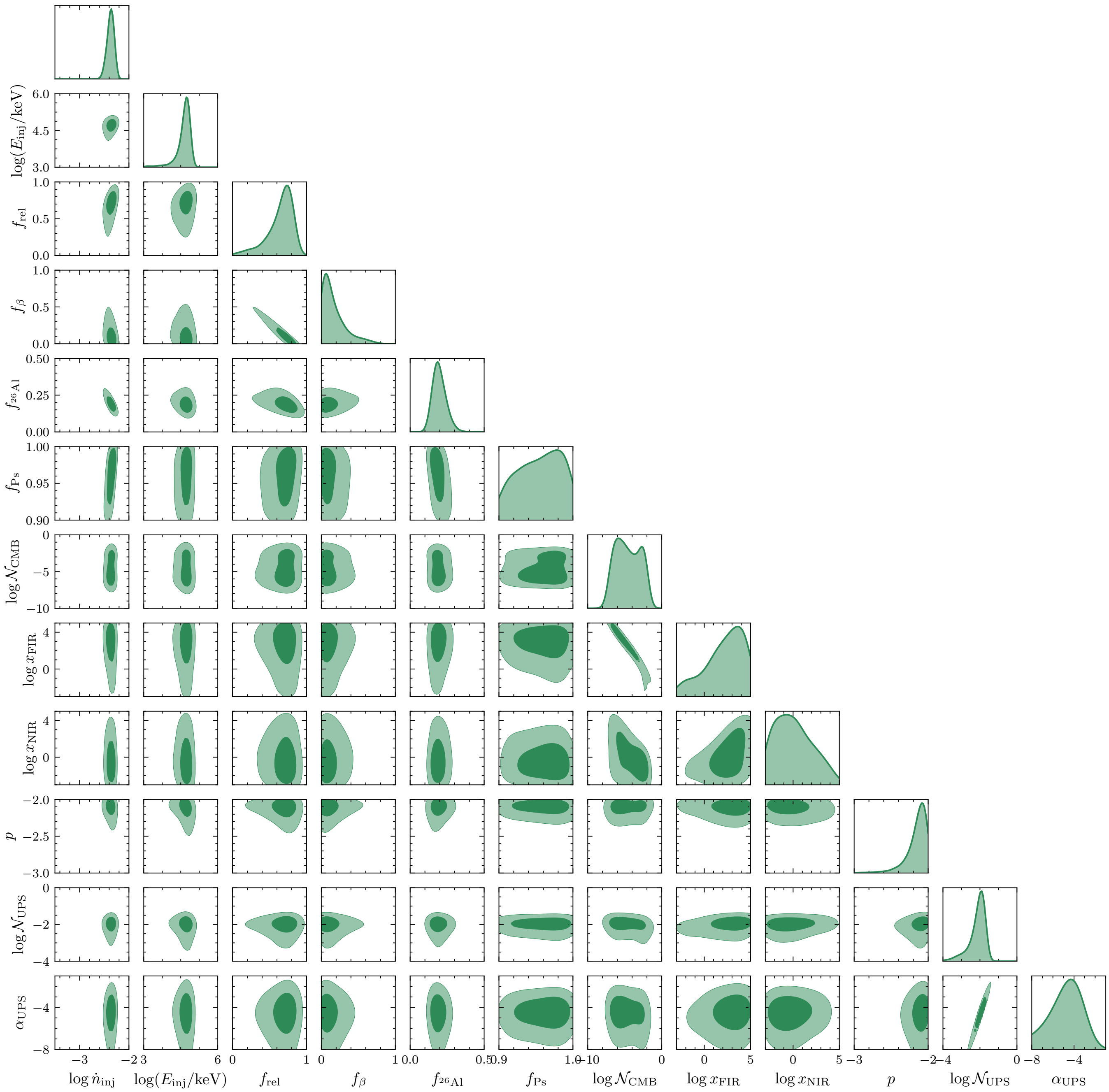

FIG. S26: Full posteriors for (V) atomic medium, $f_{\rm IC} = 10^{-6}$, for the 95° ROI.